MULTIFUNCTIONAL (NO_x/CO/O_2) SOLID-STATE SENSORS FOR COAL COMBUSTION CONTROL

Final Technical Progress Report

Start Date: September 30, 2002
End Date: March 01, 2007

Eric D. Wachsman

June 2007

DOE Award Number – DE-FC26-03-NT41614

Department of Materials Science and Engineering
University of Florida
Gainesville, FL 32611-6400

DOE Project Manager: Rick Dunst
Phone: (412) 386-6694; Email: dunst@netl.doe.gov

DISCLAIMER

ABSTRACT

Solid-state sensors were developed for coal combustion control and the understanding of sensing mechanisms was advanced. Several semiconducting metal oxides (p-type and n-type) were used to fabricate sensor electrodes. The adsorption/desorption characteristics and catalytic activities of these materials were measured with Temperature Programmed Desorption (TPD) and Temperature Programmed Reaction (TPR) experiments. The sensitivity, selectivity, and response time of these sensors were measured for steps of NO, NO_2, CO, CO_2, O_2, and H_2O vapor in simple N_2-balanced and multi-component, simulated combustion-exhaust streams. The role of electrode microstructure and fabrication parameters on sensing performance was investigated. Proof for the proposed sensing mechanism, Differential Electrode Equilibria, was demonstrated by relating the sensing behavior (sensitivities and cross-sensitivities) of the various electrode materials to their gas adsorption/desorption behaviors and catalytic activities.

A multifunctional sensor array consisting of three sensing electrodes and an integrated heater and temperature sensors was fabricated with tape-casting and screen-printing and its NO_x sensing performance was measured. The multifunctional sensor demonstrated it was possible to measure NO_2 independent of NO by locally heating one of the sensing electrodes.

The sensor technology was licensed to Fuel FX International, Inc. Fuel FX has obtained investor funding and is developing prototype sensors as a first step in their commercialization strategy for this technology.

TABLE OF CONTENTS

1. INTRODUCTION

There is a tremendous environmental and regulatory need for the monitoring and control of NO_x emissions from coal combustion [1,2,3,4]. Solid oxide electrochemical O_2 sensors are inexpensive and their performance is well demonstrated in harsh, high-temperature combustion exhaust environment. If modified to selectively measure the concentration of NO_x and CO, this type of sensor can be used to further improve combustion control, resulting in improved fuel utilization and reduced emissions.

We have developed solid-state sensor technology that can provide an inexpensive, rugged, and small solid-state device capable of measuring the concentration of multiple species (such as NO, NO_2, and CO) in coal, natural gas and oil combustion exhaust [5,6]. Our sensor technology is similar to that of conventional automotive O_2 sensors and thus can be used directly in high-temperature exhaust. However, both the sensing and reference electrode are in the same gas stream, significantly reducing fabrication costs. These small (<1 cm^2) simple potentiometric (voltage output) sensors are sensitive to each of these gases and can be readily combined on a single chip to provide a multifunctional (NO_x, CO, O_2) sensor (Fig. 1). This technology is the basis for a low cost, simplified way to meet emissions monitoring regulations as well as to improve combustion control, thus, improving fuel utilization and reducing emissions from coal combustion.

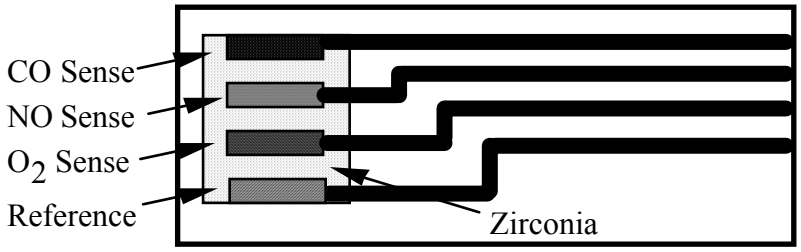

Fig. 1. Multifunctional NO_x, CO, O_2 sensor.

The key scientific issue that must be addressed for this type of sensor to effectively measure NO_x and CO concentrations in coal combustion exhaust gas streams is the selectivity of the electrode(s) for discrimination between gaseous NO_x and CO vs. O_2 [7]. Specifically, the sensors must exhibit a highly selective response to ppm levels of NO_x and CO in the presence

of percent levels of O_2. Not only must the sensor exhibit a selectivity factor based on the typical concentration differences between NO and O_2 (e.g., 1000:1 NO/O_2), but the sensor must be insensitive to large changes in the O_2 concentration associated with variations in combustion conditions [8].

An innovative scientific approach known as "Differential Electrode Equilibria" has been investigated and demonstrated for use in potentiometric gas sensors. Sensors based on this approach provide the necessary selectivity to measure, for example, ppm levels of NO with high-sensitivity in lean-burn (13 – 17 % O_2) exhaust gas unaffected by variations in O_2 concentration. The objectives of the proposed research were to advance the fundamental understanding of this approach, and apply it to the development of selective NO_2, CO, and O_2 electrode elements. Finally, the research was to culminate with the fabrication and testing of a multifunctional (NO_x, CO, O_2) sensor. In achieving these objectives, we have both advanced the science of solid-state electrochemical sensors, including the education and training of students, and brought closer to commercialization a device that will result in both improved fuel utilization and reduced emissions from coal combustion.

Differential Electrode Equilibria

A difference in electrochemical potential between two electrodes exposed to the same environment will occur if one or both of the electrodes does not achieve thermodynamic equilibrium. In a potentiometric sensor, this non-Nernstian response produces a voltage that depends on the concentration of one or more of the species present.

Semiconducting resistive sensors have been investigated for many years for detection of gases [5, 8]. Sensor characteristics depend on the microstructure of the material and geometrical configuration of the sensor element. However, most of these sensors lack the ability to selectively detect the individual gases. For instance, it is difficult to monitor NO under varying O_2 concentration in combustion exhaust using only a resistive sensor.

Traditional potentiometric sensors operate on the principle that a voltage arises between two similar electrodes, fabricated on two opposite faces of an electrolyte material, when

exposed to different environments [9]. The voltage is proportional to the log of the pO_2 difference.

In contrast, our sensors operate with two dissimilar electrodes exposed to the same environment. The differential electrode equilibria, created between the gas molecules and the dissimilar sensor electrode surfaces, give rise to a potential gradient between the electrodes resulting in a voltage response [10]. When combined with Platinum reference electrodes on YSZ substrates, devices based on semiconducting oxide electrodes are sensitive and selective to NO with negligible response to O_2 [7].

The composition and microstructure of the sensing electrode are key parameters that influence the sensing mechanism. Furthermore, the specific sensing mechanism that occurs can affect the response time, selectivity, and sensitivity performance of the sensor. We investigated the effect of electrode microstructure on the NO sensitivity and response time of La_2CuO_4-based potentiometric sensor.

Various potentiometric gas sensors based on semiconducting metal oxides have shown good sensitivity with stable response. Di Bartolomeo *et al.* reported that potentiometric planar sensors built using WO_3, $LaFeO_3$, $La_{0.8}Sr_{0.2}FeO_3$, and ZnO, where both electrodes were on the same face, showed fast and stable response to NO_2 and CO [11, 12]. Gas-sensing properties of potentiometric tubular sensors based on semiconducting metal oxides such as WO_3, SnO_2, ZnO, CdO, MoO_3, In_2O_3, etc., were also investigated [13, 14]. Among these oxides, WO_3 is of particular interest because it has been known to be sensitive to NO_x without significant sensor signal drift. According to earlier studies, the potentiometric response to NO_x using a WO_3 electrode was fast and stable. Furthermore, this type of sensor had a linear relationship between the sensor electromotive force (EMF) and the logarithm of NO_x concentration [14, 15]. However, information about its selectivity, stability, and reproducibility were not currently available. Additionally, a potentiometric La_2CuO_4 sensor showed adequate and stable response to NO_x [8]. Several other materials (e.g., Cr_2O_3, SnO_2, and CeO_2) were also evaluated as potential candidates for selectively detecting NO_x in these conditions. In evaluating the capabilities of these sensors, the critical requirement for NO_x detection in combustion exhausts containing hydrocarbons, CO_2, H_2O, O_2, CO, and NO_x is the selectivity of the electrode.

Asymmetrical potentiometric sensors based on La_2CuO_4, WO_3, Cr_2O_3, SnO_2, and CeO_2 electrodes were investigated. This report describes their sensing properties (i.e., selectivity, sensitivity, and response time) for the detection of low concentration NO_x (10 – 650 ppm) in N_2 and simulated combustion exhaust streams. Additionally, sensing mechanisms of La_2CuO_4- and WO_3-based sensors are discussed using Temperature Programmed Reaction (TPR) and Temperature Programmed Desorption (TPD) results. Finally, the results from testing of a multifunctional potentiometric gas sensor array are presented and discussed.

2. EXECUTIVE SUMMARY

General

Progress was made in developing solid-state gas sensors for coal combustion control and understanding the mechanism by which they operate. Numerous sensors were fabricated and tested to evaluate the sensing properties of different materials. The general role of electrode microstructure in sensor response was explored and identified using La_2CuO_4-based devices. Both p-type and n-type semiconducting metal-oxide NO_x sensing electrodes were developed. The adsorption/desorption characteristics and catalytic activities of these materials were measured with Temperature-Programmed-Desorption (TPD) and Temperature-Programmed-Reaction (TPR). The sensing behaviors of the various electrode materials (sensitivities and cross-sensitivities) were related to their gas adsorption/desorption behaviors and catalytic activities. The role of gas adsorption/desorption and heterogeneous catalysis in the sensing results was repeatedly observed, which further supports the proposed "Differential Electrode Equilibria" theory. To conclude this work a multifunctional sensor was fabricated and shown to be selective to NO_2 over NO and total NO_x, providing a single device that can detect the individual constituents of NO_x. During the course of this work twelve scientific articles were accepted or published. The sensor technology was licensed to Fuel FX International, Inc. Fuel FX has obtained investor funding and is developing prototype sensors as a first step in their commercialization strategy for this technology.

Sensor Optimization (Electrode Materials)

NO_x sensors based on La_2CuO_4 were tested in single component N_2-balanced and multi-component simulated combustion exhaust streams containing N_2, CO_2, H_2O, O_2, CO, and NO_x. The sensors showed high selectivity toward NO_x between 400 and 600 °C. The NO sensitivity (i.e., voltage response to a ppm change in gas concentration) increased with decreasing temperature. However, at lower temperatures the sensing response was slow and irreversible. An abrupt decrease in sensitivity occurred above 500 °C, while at 350 ºC the response saturated. Both of these phenomena are in good agreement with changes in adsorption/desorption behavior observed from TPD results. This indicates that NO sensing from La_2CuO_4 is likely due to the chemisorption of NO and the resulting change in Fermi level of the oxide.

The sensitivities of the p-type La_2CuO_4-based sensors for NO_2 and CO were also high, but for CO_2 and O_2 they were negligible. As in the case for NO, the sensitivity of the sensors toward NO_2 and CO increased at lower temperatures at the expense of response kinetics. The responses to the reducing gases NO and CO were positive and the responses to NO_2, an oxidizing gas, were negative.

In contrast to La_2CuO_4, n-type WO_3-based sensors had positive responses to NO_2 and negative responses to NO at 650 °C. The WO_3-based sensor responded highly to about 10 ppm NO_2 and was selective even when CO, CO_2, and H_2O were introduced. The NO_2 sensitivity changed only slightly in simulated exhaust gas. The presence of H_2O and CO, however, did have an effect on NO sensitivity. The sensor response to NO in simulated exhaust gas was considerably different from that in 3 % O_2. These results indicate that the WO_3-based sensor might be used to selectively monitor NO_2 in these conditions.

The NO_x selectivity of Cr_2O_3, SnO_2, and CeO_2 electrodes was also measured. The NO_2 sensitivity of all three of the electrode were unaffected by the presence of 0 to 200 ppm of CO or % levels of CO_2. The NO_2 sensitivity of the electrodes changed significantly when the concentration of O_2 or moisture was changed.

For all the sensor materials investigated, linear relationships were obtained in the plots of the sensor voltage vs. the logarithm of NO_x concentration for both NO and NO_2. This type of relationship is advantageous and can allow gas concentrations to be determined from simple linear algorithms.

Theoretical Contribution ("Differential Electrode Equilibria" Theory)

The proposed theory, "Differential Electrode Equilibria," was demonstrated with the occurrence of various mechanisms for different electrode materials, gases, and temperatures. For example, the p-type La_2CuO_4-based sensors responded **positively** to *reducing* gases and **negatively** to *oxidizing* gases, whereas sensors based on n-type WO_3 and SnO_2 both responded **negatively** to *reducing* gases and **positively** to *oxidizing* gases. This difference is related to how the Fermi level changes during the adsorption or catalysis of gas on an electrode and is dependent on that material's electronic structure. This contribution to the electrode potential is not considered in Mixed Potential theory. In fact, according to Mixed Potential Theory, gases are electrochemically reacted on electrodes at the triple phase boundary. However, in the TPR measurements NO was not converted to NO_2 for any of the electrode materials, including the most catalytic (Platinum), as is commonly assumed in the literature.

The desorption profile of NO on La_2CuO_4 illustrates that NO must adsorb/desorb during potentiometric NO sensing. NO does not fully desorb from the surface of La_2CuO_4 until temperatures above 400 °C. Therefore, the sensor response is unstable below 400 °C because the metal-oxide surface is saturated with adsorbed gas. That is, below 400 °C the rate of NO adsorption is greater than the rate of NO desorption. In this case, the sensing mechanism is dominated by adsorbed NO species that are not in full equilibrium with the gas phase. This is most likely by a semiconducting response (change in Fermi level) rather than heterogeneous kinetics (Mixed Potential). Above 400 °C, the rate of NO desorption is greater than the rate of NO adsorption, and any surface NO species are now directly proportional to the gas-phase composition. The lack of any NO_2 from co-adsorbed NO and O_2 would tend to indicate that the sensor response is not due to the conventional Mixed Potential theory.

The n-type semiconducting WO_3-based sensor showed optimal NO_2 sensing behavior at 650 ºC and the response decreased with increasing temperature. This temperature effect can be explained using the NO_2 TPR results. There was a temperature-dependent dissymmetry in the catalytic activity for NO_2 reduction between the WO_3 and Pt (reference) electrodes. This dissymmetry translates to different rates for the individual electrodes to reach a steady-state potential. Because this difference in catalytic activity increases with temperature, the NO_2 response is decreased at high temperatures.

When a sensor is subjected to a change in gas composition, the potentials of the electrodes change for various reasons. Differential Electrode Equilibria says that multiple sources may contribute to the change in potential of an individual electrode and that the device response depends on the difference between the two electrode potentials. Electrochemical reactions (Mixed-Potential) may establish some of the sensor responses but cannot explain all observed sensing behavior. Differential Electrode Equilibria presents a more comprehensive sensing

mechanism with the consideration of changes in sensor response due to electrode semiconducting character, heterogeneous catalysis, and electrochemical reactions.

Sensor Optimization (electrode microstructure and catalysts)

The effect of electrode grain size on NO_x sensitivity and response time was investigated using a La_2CuO_4-based potentiometric sensor. Large surface area powders generated porous electrode morphologies with small grain sizes. Furthermore, fine-grained electrodes exhibited sharp, faster responses compared to coarse-grained electrodes. Sintered electrodes with a finer grain distribution exhibited larger responses at low gas concentrations and faster response times.

Multifunctional Sensor

Several approaches were identified for increasing the selectivity of potentiometric sensors. However, NO vs. NO_2 selectivity was a problem for all sensing electrode materials investigated. To solve this problem a device can contain multiple sensing electrodes with at least one electrode heated locally in order to reduce its NO sensitivity.

A multifunctional sensor array was fabricated and tested in NO_x containing atmospheres. The sensor was fabricated via tape-casting, screen-printing, and simple sintering in air. A local heating structure and temperature sensors were incorporated into the sensor with additional screen-printing and sintering steps. The prototype sensor array contained two sensing electrodes, which were both referenced to a porous Platinum electrode. One sensing electrode was locally heated to improve its NO_2 vs. NO selectivity, while the other remained at a temperature where it was sensitive to both NO and NO_2. A device such as this was used to determine individual concentrations of NO and NO_2 while consuming only about 360 mW at 3.5 V for local heating.

3. EXPERIMENTAL

3-1. Electrode Powder Synthesis/Procurement

3-1-1 WO_3

Tungsten oxide (WO_3, 99.8 % purity, Alfa Aesar) was purchased from a standard chemical reagent supplier. The as-received powders were then vibratory milled in isopropanol reducing their particle size from 5 μm to between 100 and 200 nm.

3-1-2 SnO_2, CeO_2, and Cr_2O_3

Chromium oxide (Cr_2O_3), tin oxide (SnO_2), and cerium oxide (CeO_2) powders were synthesized with wet-chemical techniques. Chromium oxide and tin oxide were prepared by thermal decomposition of $SnCl_2$ (Fisher Scientific, anhydrous) and $CrCl_2{\cdot}_6H_2O$ (Johnson Matthey Electronics), respectively, at 600°C for 5h. Cerium oxide precipitate was produced from $Ce(NO_3)_3{\cdot}6H_2O$ (Alfa Aesar, 99.5 %) in H_2O with the addition of ammonia until the pH reached 7. The resulting precipitate was then calcined at 600°C for 5 h.

3-1-3 La_2CuO_4

La_2CuO_4 precursors were synthesized with the auto-ignition (amorphous-citrate) [16], Pechini [17] and co-precipitation [18] techniques in an effort to ultimately fabricate sensor electrodes with high surface/bulk ratios. These precursors were then calcined to produce phase-pure nanoscale oxide powders.

In the auto-ignition process, Lanthanum nitrate, Copper nitrate, and citric acid were dissolved in deionized H_2O and subsequently heated with thorough mixing to form a gel. This gel was burnt, forming an ash that eventually calcined to form La_2CuO_4. The nature of the burning depends on the citrate-nitrate ratio (γ), the key to controlling the final powder morphology. The nitrate and citrate ions in the gel undergo a redox reaction in the presence of sufficient heat (~ 175 °C) [19]. The coefficients of the reaction dictate that the molar ratio of citrate ions and nitrates ions is $\gamma = 0.277$ for the stoichiometric condition. Excess citric acid in

the gel ($\gamma > 0.277$) represents a fuel-rich condition, while lower concentrations produce a fuel-lean condition. Two different ratios were adopted to produce powders which are named as auto-ignition fuel-lean ($\gamma = 0.098$) and auto-ignition fuel-rich ($\gamma = 0.50$), respectively. Such conditions were expected to produce perovskite powders with different properties and varying particle characteristics.

In the co-precipitation process, aqueous 1:1 metal stoichiometric solutions of the metal nitrates were prepared in distilled H_2O. The metals were precipitated as hydroxides by slowly adding 10 % excess of a basic solution of tetra-methyl ammonium hydroxide in 25 % methanol. The precursor metal-hydroxide powders were recovered, rinsed, and air-dried at 110 ºC overnight.

In the Pechini process, a solution was formed from citric acid, ethylene glycol and cation nitrate salts. The solution was heated and formed a gel, which was subsequently burnt.

3-2. Physical Characterization Techniques

X-Ray powder diffraction (XRD) was utilized to characterize the synthesized metal oxide (MO_x) powders. A Philips APD 3720 automated diffractometer (Cu Kα radiation, $\lambda = 1.54178$ Å) was used to confirm the phase homogeneity of the oxide powders. The powders were imaged with a high-resolution Field-Emission Scanning Electron Microscope (FE-SEM) to determine the primary particle size and agglomerate structure. The specific surface areas of the powders were measured with BET N_2-adsorption.

3-3. Potentiometric Sensor Fabrication

Sensors were fabricated as described in the previous reports and shown in Fig. 2. The sensors were built using 8-mole % Y_2O_3-doped ZrO_2 substrates (Marketech International Inc., YSZ-8Y, 20 × 12 × 0.1 mm) as solid electrolytes, and metal-oxide layers (MO_x, where MO_x = WO_3, Cr_2O_3, SnO_2, CeO_2, or La_2CuO_4) and Platinum layers as electrodes.

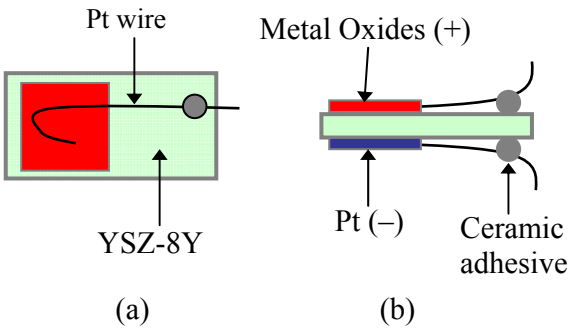

Fig. 2. Schematic diagram of a potentiometric sensor. (a) Top view, (b) Side view.

For the preparation of sensing electrodes, metal oxide powders were mixed with ethanol and polyethylene glycol 400 (PEG-400, Avocado Research Chemicals Ltd.) and subsequently ball-milled for 24 h. The mixed slurry was then heated at 60 °C for 10 h to completely remove the ethanol. One face of the YSZ-8Y substrate was screen-printed with the La_2CuO_4 (or other MO_x) slurry and the other with platinum paste (Heraeus, Conductor paste CL11-5349). Platinum wires (dia. = 0.127 mm) were connected to both electrodes. After securing the ends of Platinum wires with high temperature adhesive (Aremco Products Inc., Ceramabond 571-VFG-P), the sensor electrodes were sintered at 800 °C for 10 h with heating and cooling rates of 5 °C/min. Micrographs of the sintered sensing electrodes were obtained using a scanning electron microscope (SEM, JEOL JSM 6400).

3-4. Measurements of Sensing Properties

An apparatus for the sensor measurements was constructed using a gas-tight quartz tube. The sensor was installed in the tube in such a way that both electrodes were exposed to the same gas atmosphere. The electrodes were then connected to a Keithley 2000 multimeter for the measurements of electromotive force (EMF) ((–) Pt/YSZ-8Y/MO_x (+)). A Eurotherm 2408 temperature controller was used to operate a furnace, which enclosed the quartz tube containing the sensor. The flow rates of the gases were controlled using mass flow controllers (MFCs, MKS Instruments Inc.). The total gas flow rate was fixed at 300 cc/min. The gas stream was humidified with a water bubbler. Custom software (Labview 7.1) controlled the overall experiments through GPIB and RS-232 communication ports.

The sensor was allowed to equilibrate with an initial gas environment of 3 % O_2 in N_2 or simulated combustion exhaust gas (16 % CO_2, 100 ppm CO, 3 % O_2, and 3 % H_2O). The sensor EMF was measured with increasing and then decreasing concentration steps of NO_x. The retention time at each step was 200 to 300 s. First, the EMF changes were recorded as a function of temperature from 300 to 800 °C, while varying the concentration of NO_x from 0 to 650 ppm. Then, the selectivity for NO_x vs. CO, CO_2, O_2, and H_2O was investigated both in 3 % O_2 with N_2 balance and in the simulated combustion exhaust environment.

3-5. TPR/TPD Experiments

Gas reactions catalyzed by the WO_3 powder (W), the WO_3 film on the YSZ-8Y (W+Y), the Platinum on the YSZ-8Y (Pt+Y), the YSZ substrate alone (Y), and the La_2CuO_4 powder were analyzed using the temperature-programmed reaction (TPR) technique. Additionally, the TPR experiments were performed using a blank reactor (B) to determine the uncatalyzed reaction products, if any. Initially, 500 to 2000 ppm of the reactant gases or the gas mixtures was flown at 30 cc/min through the reactor, which was held at 50 °C. When the gas flow was stabilized, the temperature was increased from 50 to 800 ºC at 30 ºC/min while measuring the concentrations of the effluent gases with a quadrupole mass spectrometer (QMS, Extrel). The QMS scanned for carbon fragments (m/e = 12), nitrogen fragments (m/e = 14), CO (m/e = 28), NO (m/e = 30), O_2 (m/e = 32), CO_2 (m/e = 44), N_2O (m/e = 44), and NO_2 (m/e = 46) during the TPR measurements.

The Temperature-Programmed Desorption (TPD) experiments were performed to investigate the adsorption characteristics of NO, CO, O_2, CO_2, and their mixtures on samples of La_2CuO_4 powder (mass = 0.033 g, total BET surface area ≈ 0.066 m^2). The TPD experiments began with the adsorption of a particular gas (or gas mixture) at 300 ºC for 30 min. The reactor was then cooled down to 30 ºC at 5 ºC/min. Upon reaching 30 °C, the reactor was purged with Helium containing 1 % Argon for the purpose of internal calibration. The temperature was then increased to 800 ºC under flowing (30 cc/min) Helium, while the QMS measured the desorption products.

3-6. Multifunctional Sensor Fabrication and Experiments

3-6-1. Preparation of YSZ substrates

8 mol % yttria stabilized zirconia (YSZ) substrates for the multifunctional sensor were prepared by a tape-casting technique. The fabrication of the YSZ substrates consists of many processing steps, as indicated in Fig. 3.

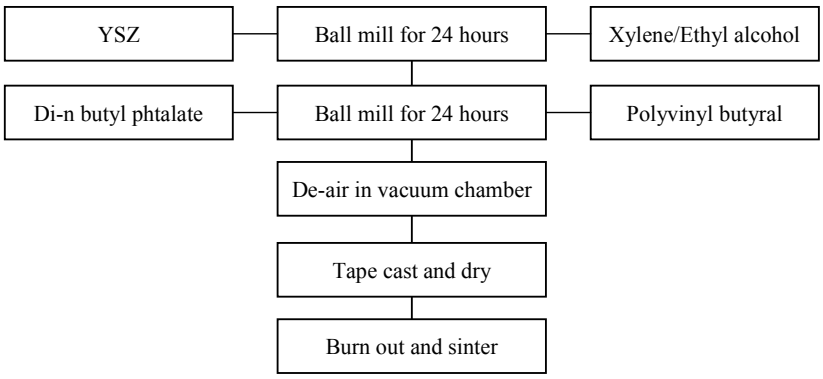

Fig. 3. Process flowchart for YSZ substrate fabrication using the tape cast technique.

YSZ powder was ball milled with a mixture of Xylene/Ethyl alcohol solvent for 24 hours in a Nalgene Polypropylene milling jar with high-purity yttria stabilized zirconia ball media. After the first ball milling step, a mixture of Di-n butyl phthalate (DBP) and polyethylene glycol (PEG) as the plasticizer and polyvinyl butyral (PVB) as the binder were added to the suspension and milled for another 24 hours to form the YSZ slurry. Air bubbles, which are entrained during milling processes, cause defects, such as pinholes and cracking, in the tape-cast products. In order to prevent these defects, the slurry was transferred to a vacuum chamber for a de-airing process which eliminated any trapped air bubbles. Finally, tape-casting was performed on a lab-scale table top continuous tape caster (Fig. 4).

Fig. 4. A lab-scale table top continuous tape caster.

3-6-2. Multifunctional Gas Sensor Array

Gas sensor arrays were constructed with multiple NO_x sensing electrodes on the tops of YSZ substrates. Heating elements and temperature sensors were integrated into the bottoms of the substrates. Various Platinum elements with different line widths were screen-printed in serpentine and C-shaped patterns on planar YSZ substrates. This was done to explore the best way of obtaining a uniform temperature distribution with low applied power. Though many patterns were tested, the C-shaped patterns proved easiest to fabricate and were used in the initial gas sensor array prototypes. The heating elements were sintered at high temperature to allow for good adhesion and conduction pathway. After Platinum leads were attached, a final sintering step was performed at a lower temperature for the electrodes.

Many samples were made with four Platinum elements on the back, but for initial experiments only three were used (one heater/temperature sensor and two temperature sensors). Two La_2CuO_4 (LCO1 and LCO2) sensing electrodes and a Platinum reference electrode were hand-painted or screen-printed on the opposite side of the YSZ substrates. The electrodes were arranged so that they were aligned with the centers of the Platinum elements. Fig. 5 shows a top view and cross-section of the array.

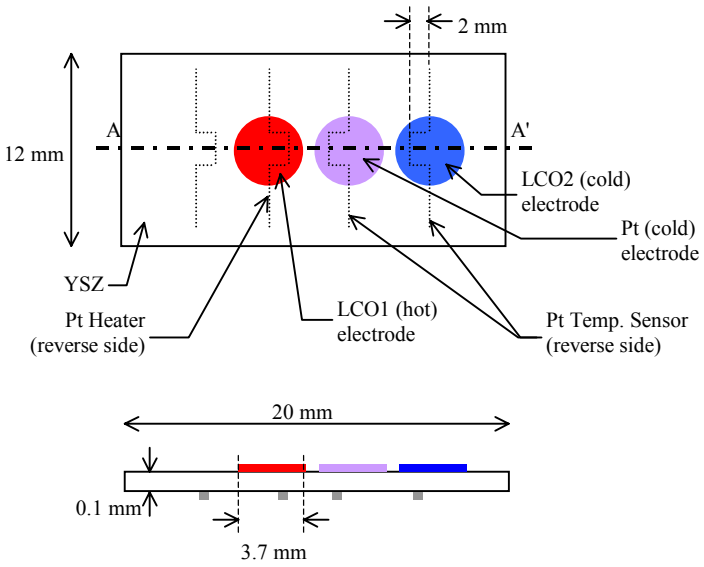

Fig. 5. Schematic of gas sensor array showing top view and cross-section A-A'.

The Platinum elements were calibrated using custom software (Labview 7.1). The software also calculated temperatures for each electrode during the ramping of the heater and sensor tests. The array was initially tested at 450 °C, 500 °C, and 550 °C to gauge performance with all electrodes at the same temperature. Once repeatability and stability were confirmed, the different coplanar sensing electrodes were tested with the heater on the opposite side. Calculated temperatures from the Platinum elements agreed well with results from Finite Element Model (FEM) calculations for the appropriate geometries and material properties. The results of these experiments showed that individual concentrations of NO and NO_2 can be determined using a single device. Efforts are currently underway to extend this approach to sensing electrode materials other than La_2CuO_4 in order to have a single gas sensor array that can detect NO_x, CO, and O_2.

4. RESULTS AND DISCUSSION

4-1. La_2CuO_4-based Sensors

4-1-1. Powder Characterization

X-ray diffraction patterns (Fig. 6(a)) of powders prepared by the different synthesis techniques showed that the minimum calcination temperature for complete phase formation of La_2CuO_4 is 600 °C (10 h) for the auto-ignition powders. At 650 °C (10 h) the co-precipitated powders were phase pure. However, even at 650 °C the Pechini powders were not phase pure. BET surface area analysis (Fig. 6(b)) shows the highest surface area was obtained with the auto-ignition fuel-rich process.

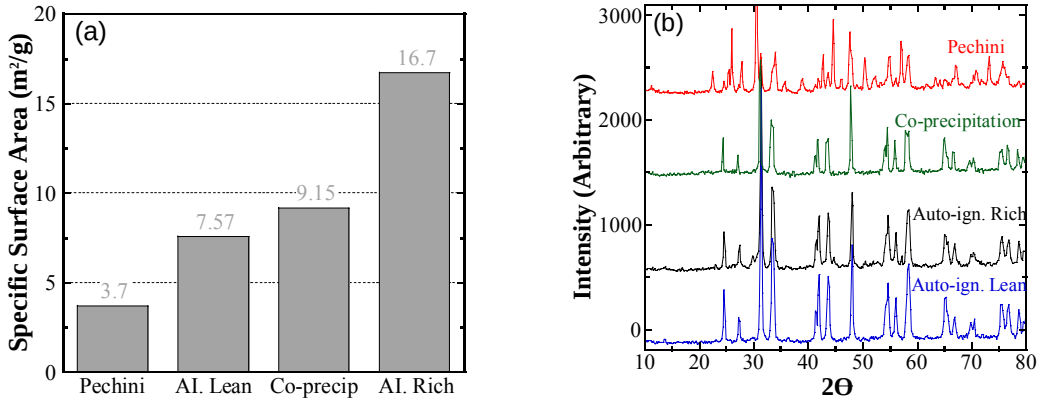

Fig. 6. Characterization of electrode powders prepared through different synthesis routes. (a) X-Ray diffraction pattern, (b) BET surface area.

Field-Emission Scanning Electron Microscope (FE-SEM) images of powders prepared through the different techniques are presented in Fig. 7. The average particle size ranges between 50 and 200 nm, depending on the synthesis technique, which were estimated from the micrographs and presented later in Table 1. Typical agglomerated structures of the respective powders are shown in the low magnification figures inside a box within the individual pictures.

The morphologies of the agglomerates, after calcination, were dependent on the method of powder synthesis. Powders synthesized with the auto-ignition fuel-rich technique were made up of submicron particles that had joined together to form net-like structures. The co-

precipitated powders were also net-like agglomerates with larger particles. The nature of agglomeration for the auto-ignition fuel-lean process was similar to that of the fuel-rich process. Conversely, the Pechini process produced an entirely different agglomerated microstructure that contained solid lumps of particles sintered together. Typical agglomerate sizes are also presented in Table 1. During sintering, the agglomerated structures result in different microstructural development, resulting in different morphologies of the sintered electrodes.

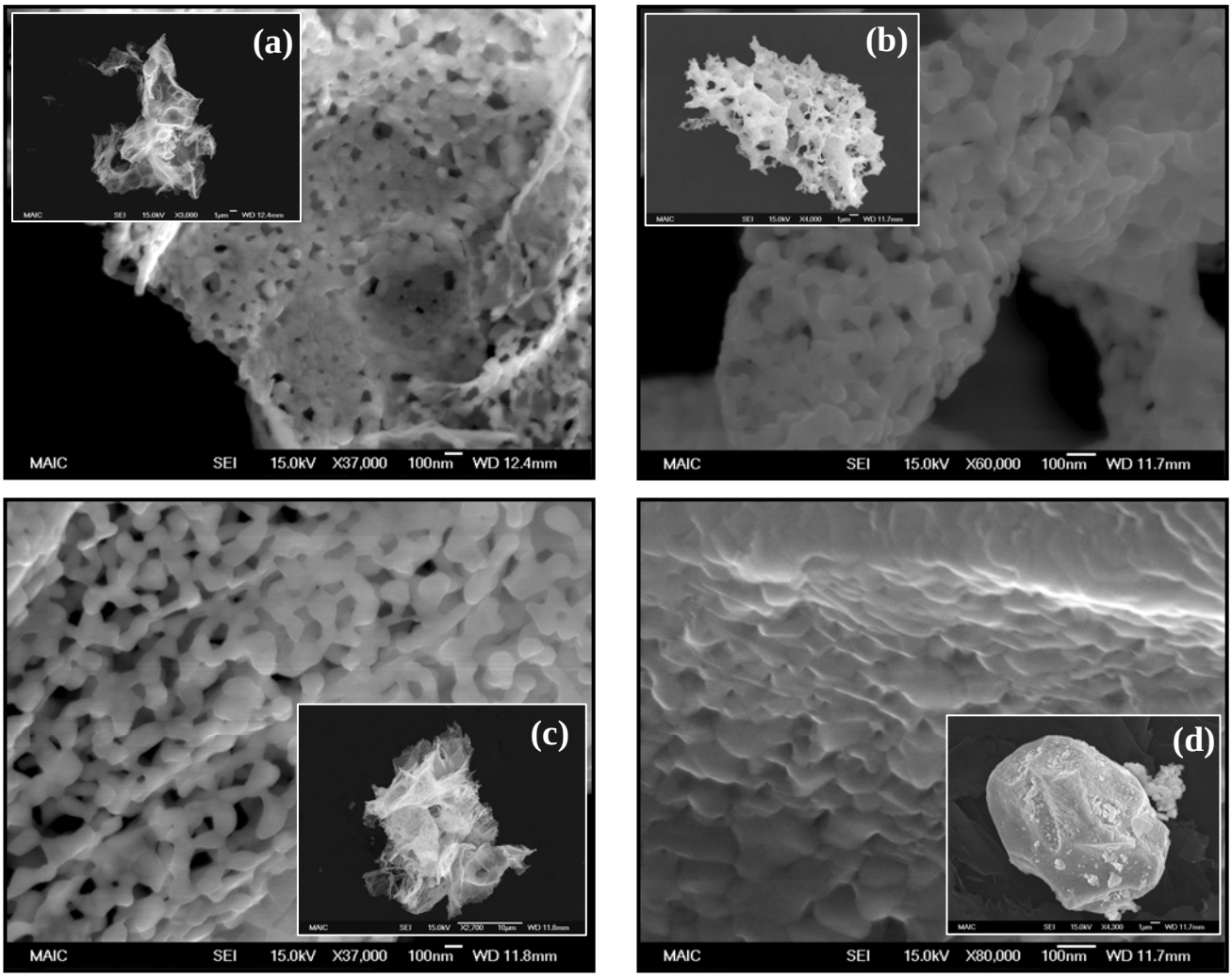

Fig. 7. Field Emission Scanning Electron Micrographs of calcined powders. (a) the auto-ignition, fuel-rich process, (b) the auto-ignition, fuel-lean process, (c) co-precipitation, and (d) the Pechini method.

Average particle size was determined from analysis of FE-SEM micrographs of the calcined powders. Among the more open net-morphology agglomerates, the lowest particle

sizes were obtained from the powders prepared through the auto-ignition fuel-rich technique. The small particle sizes of the auto-ignition powders might be related to an inherent characteristic of the synthesis process.

The Pechini prepared powders appear to have the smallest particle size. However, the higher packing density of these agglomerates makes quantitative assessment of particle size more difficult. Moreover, the BET results indicate that the Pechini processed powders should have the larger particle size. These results are summarized in Table 1.

Preparation Routes	**Calcination Condition**	**Agglomerate Size (μm)**	**Average Particle Size (nm)**	**Morphology (appearance)**	**BET Surface Area (m^2/g)**
Auto-ignition rich	600 °C / 10 h	24 ± 8	75 ± 25	Flakes	16.7
Auto-ignition lean	600 °C / 10 h	19 ± 5	85 ± 50	More spherical	7.57
Co-precipitation	650 °C / 10 h	35 ± 5	140 ± 50	Net-like	9.15
Pechini	650 °C / 10 h	17 ± 2	62 ± 12	Spherical	3.7

Table 1. Characteristics of powders prepared through different processing techniques.

4-1-2. Electrode Characterization

The sintered electrode microstructures obtained from each of the powder synthesis techniques were studied with Scanning Electron Microscopy (SEM). An SEM micrograph is shown in Fig. 8 for each of the sensor electrodes that were prepared. Each electrode was prepared by screen-printing an ink using La_2CuO_4 synthesized with a particular technique and all were subsequently sintered at 800 °C. Powders prepared through the fuel-rich auto-ignition process developed into the finest microstructures (Fig. 8(a)) with an average particle size of approximately 0.15 μm and a flakey microstructure. The fuel-lean conditions produced a comparatively coarser microstructure (Fig. 8(b)) with an average particle size of about 0.29 μm. The co-precipitation (Fig. 8(c)) and Pechini (Fig. 8(d)) processed powders similarly resulted in approximately 0.29 μm grains, but with some differences in their

microstructures.

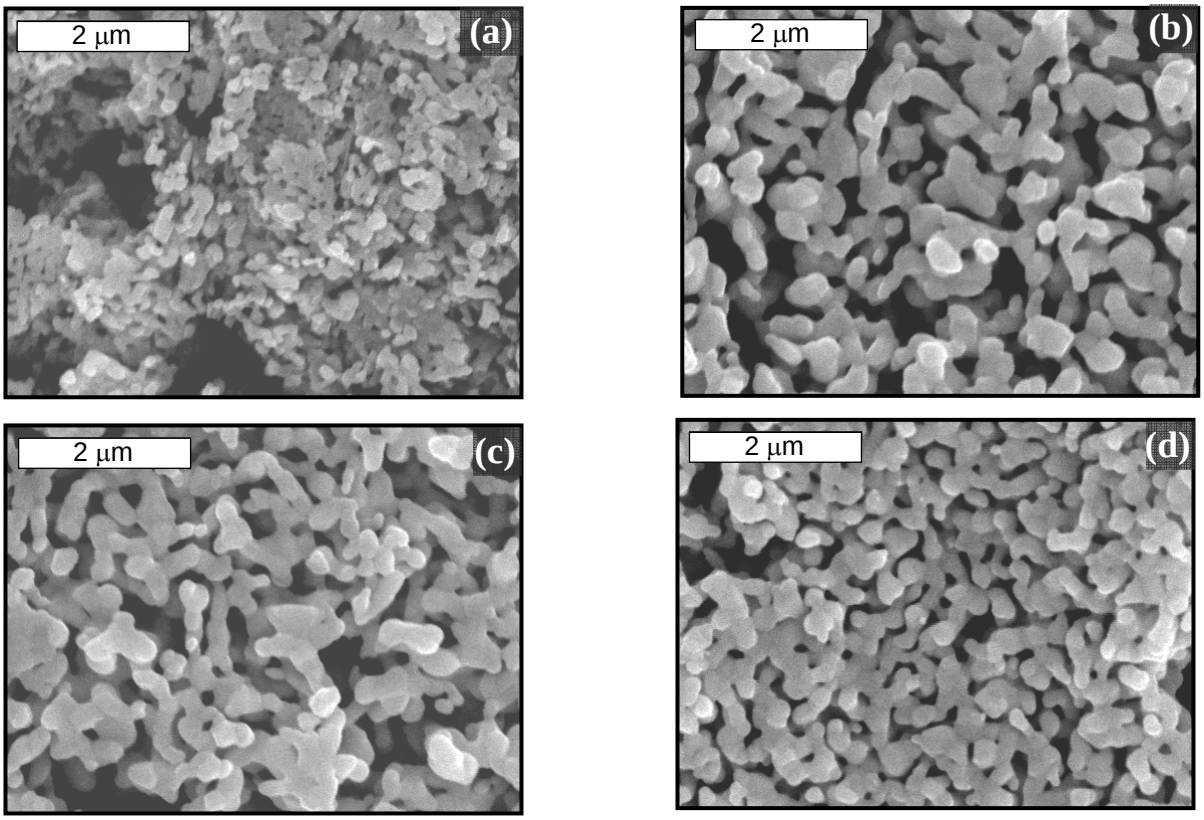

Fig. 8. Morphology of sintered sensing electrodes prepared by screen-printing ink contain La_2CuO_4 powders synthesized with different techniques. (a) The auto-ignition, fuel-rich process, (b) the auto-ignition, fuel-lean process, (c) co-precipitation, and (d) the Pechini method. All electrodes were sintered at 800 °C for 10 h.

The effect of sintering temperature was studied with the co-precipitated powders. SEM micrographs of the co-precipitated powders that were sintered at four different temperatures are presented in Fig. 9. The figure shows a limited increase in grain size between 700 and 800 °C, followed with a dramatic increase in grain size beyond 800 °C. At 1050 °C, the grains are very large, more joined together, and have a large reduction in contact angle between the grains.

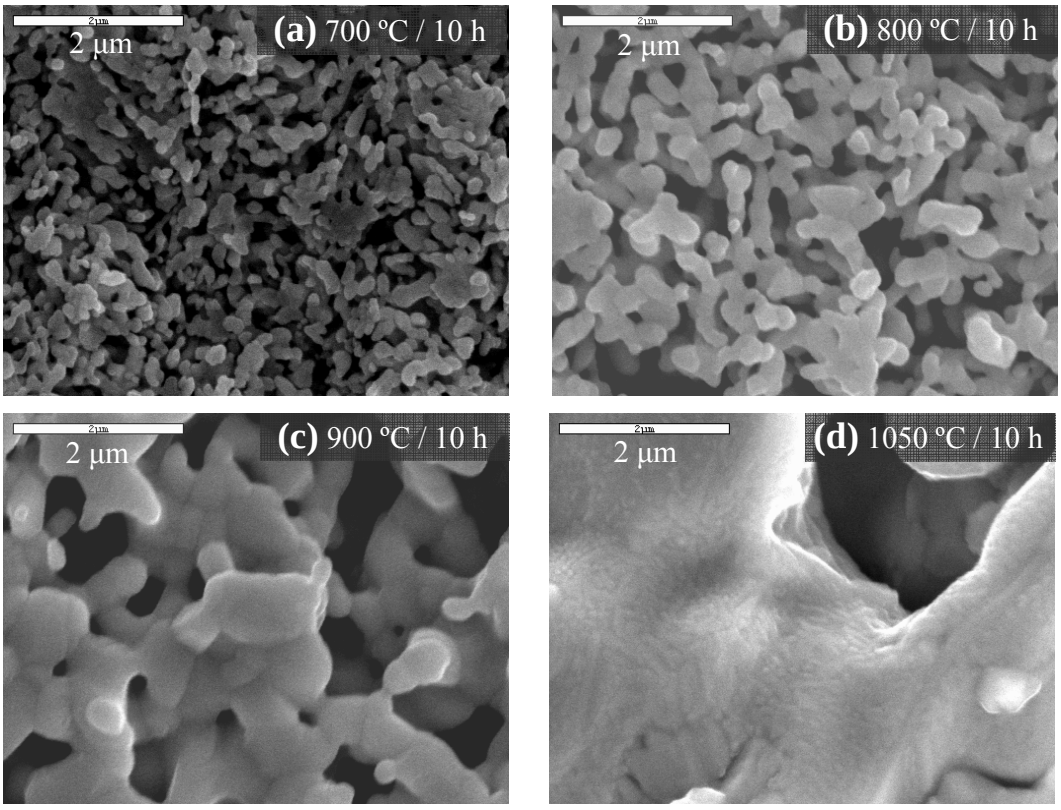

Fig. 9. Variation in microstructure for electrodes prepared with co-precipitated La_2CuO_4 powder and sintered at various temperatures: (a) 700 °C/10 h, (b) 800 °C/10 h, (c) 900 °C/10 h, and (d) 1050 °C/10 h.

Similar variations with sintering temperature were observed for powders produced through the other three different synthesis routes. Some of the microstructures are presented in Fig. 10, showing variation of morphology with sintering temperature and time.

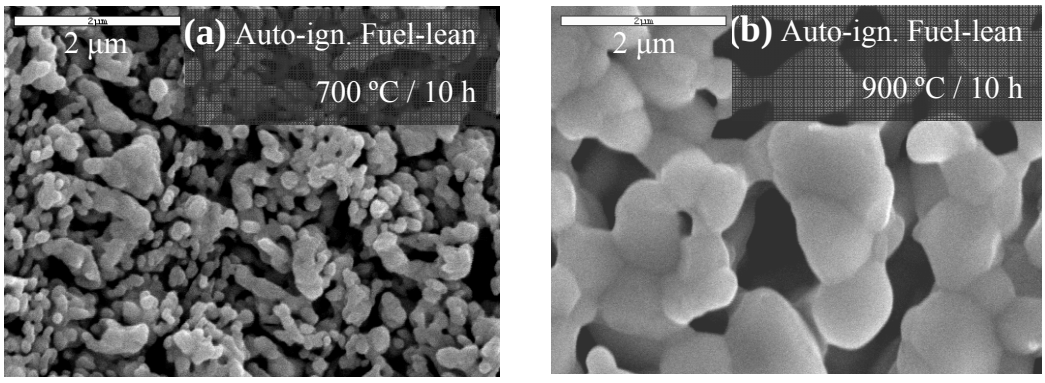

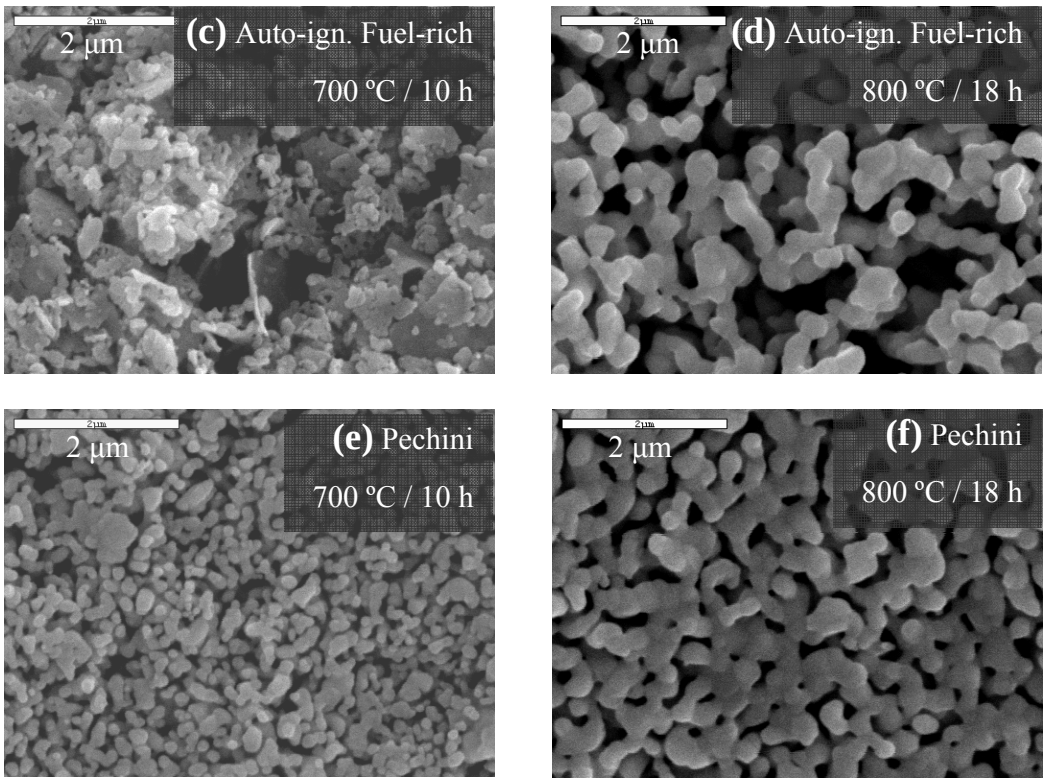

Fig. 10. Variation of microstructure of electrode material sintered at various temperatures and processes. Auto-ignition Fuel-lean at (a) 700 °C / 10 h and (b) 900 °C / 10 h; Auto-ignition Fuel-rich (c) 700 °C / 10 h and (d) 800 °C / 18 h; Pechini (e) 700 °C / 10 h and (f) 800 °C / 18 h.

Powders prepared with other techniques also have limited grain growth up to 800 ºC, which can be seen by comparing Fig. 10(c) (700 ºC / 10 h) and Fig. 8(a) (800 ºC / 10 h) for auto-ignition rich powders, and relatively large grain growth at 900 ºC and above. The effect of sintering time is less of an issue, although there is some grain growth between 10 h and 18 h of sintering at 800 ºC as presented in Fig. 8(a) (800 ºC/10 h) and Fig. 10(d) (800 ºC / 18 h) for auto-ignition rich powders, and Fig. 8(d) (800 ºC / 10 h) and Fig. 10(f) (800 ºC / 18 h) for Pechini powders. Based on these observations, the temperature of sintering was selected to be 800 ºC for 10 h, yielding a small-sized and uniform distribution of grains and pores.

4-1-3. Effect of Microstructure on the Sensing Properties

The sensor responses at 450 and 500 °C for the samples prepared with the different powders are compared in Fig. 11. The auto-ignition powders showed the sharpest response,

and this was more evident at the lower operation temperature. This may be due to the flaky grains having higher available surface area (Fig. 11(a)) for the gas species. Samples prepared from Pechini powders showed the highest sensitivity (~ 20 mV at 650 ppm of NO), whereas co-precipitated powders showed the lowest sensitivity (~ 13 mV at 650 ppm of NO) at 450 °C. However, at 500 °C, co-precipitation and auto-ignition lean exhibited the greatest sensitivity.

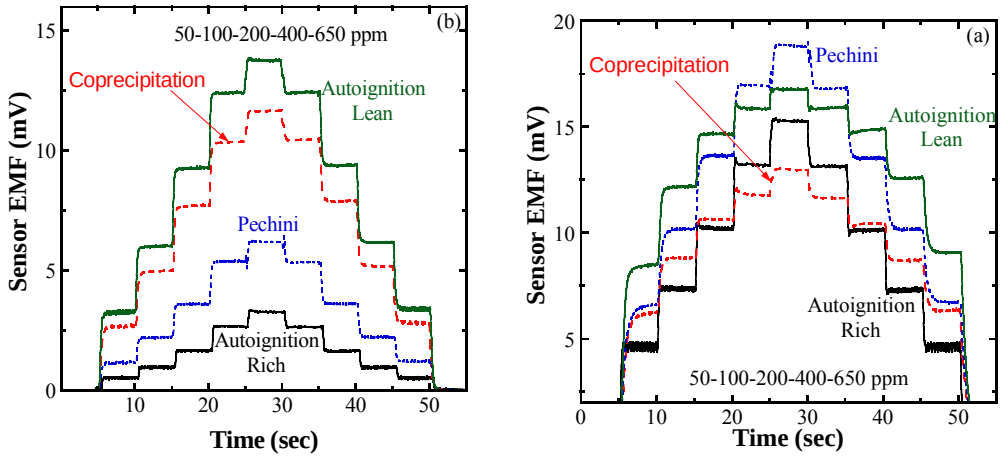

Fig. 11. Response for NO sensors fabricated through Pechini, Auto-ignition Lean, Auto-ignition Rich, and Co-precipitation processes, at (a) 450 ºC and (b) 500 ºC in simulated exhaust.

The temperature dependence of sensor response for the samples prepared from the different powders is shown in Fig. 12. Among these samples, the sensors prepared from Pechini processed powders have the strongest temperature dependence. The results also show that the sensitivity increases at lower operating temperatures.

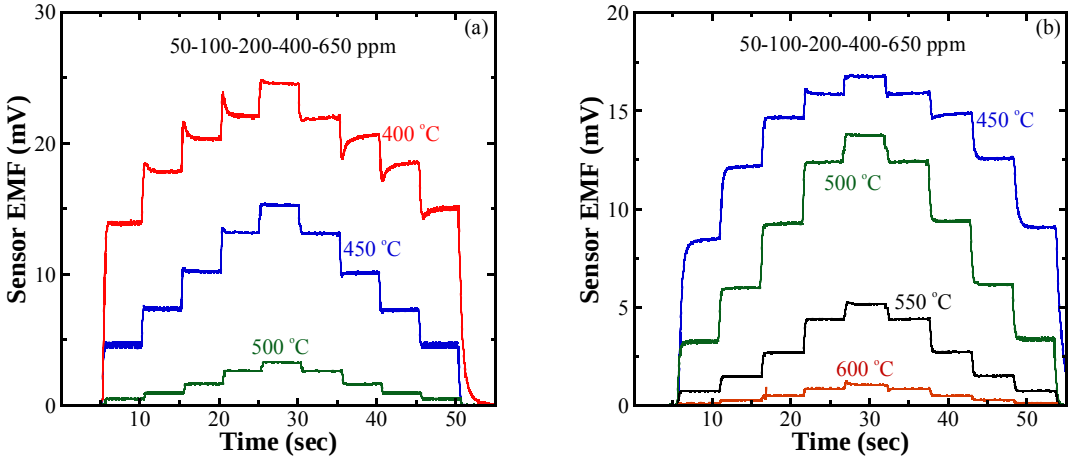

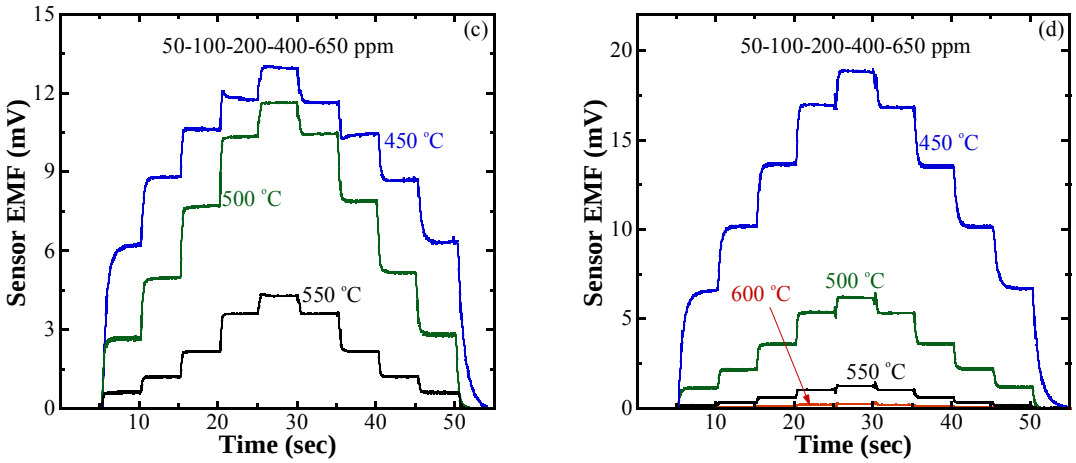

Fig. 12. Sensor response to NO at varying measurement temperatures for powders prepared through different processes (all sintered at 800 °C/10 h). (a) Auto-ignition Rich, (b) Auto-ignition Lean, (c) Co-precipitation, and (d) Pechini.

Response stability is defined as the qualitative assessment of the rise and fall of sensor voltage with each concentration step. A stable response occurs if there is a rapid vertical rise (or fall) followed by a 90° transition and flat plateau region. The response stability decreased at the lower limit of the operating temperatures that were investigated. Of all the samples tested, only the auto-ignition rich prepared electrodes had reasonable stability down to 400 °C. However, these sensors overshot their steady-state responses at 400 °C, which indicates that there was indeed a decrease in stability (Fig. 12(a)).

At lower measurement temperatures, the sensitivity at lower gas concentrations also increased. The range of maximum sensitivity for detection of NO gas concentration was also dependent on the powder synthesis route. The auto-ignition rich samples were highly sensitive between 0 and 50 ppm, whereas samples prepared from the Pechini process were more sensitive to higher ppm ranges. Correlating these results with microstructures (Fig. 8) of corresponding samples, it may be concluded that improved sensor resolution at lower ppm ranges can be achieved with finer microstructural features.

The sensor responses to each NO concentration from Fig. 12 were averaged for two runs of increasing and decreasing gas steps and are plotted in Fig. 13(a) and (b). At 450 °C, auto-ignition lean and Pechini prepared electrodes exhibited higher voltage responses. Also at this

temperature, the sensitivity to changes in NO concentration was non-linear for auto-ignition lean and co-precipitation prepared electrodes. At 500 °C, the auto-ignition lean and co-precipitation samples are most sensitive and the sensitivity is more linear.

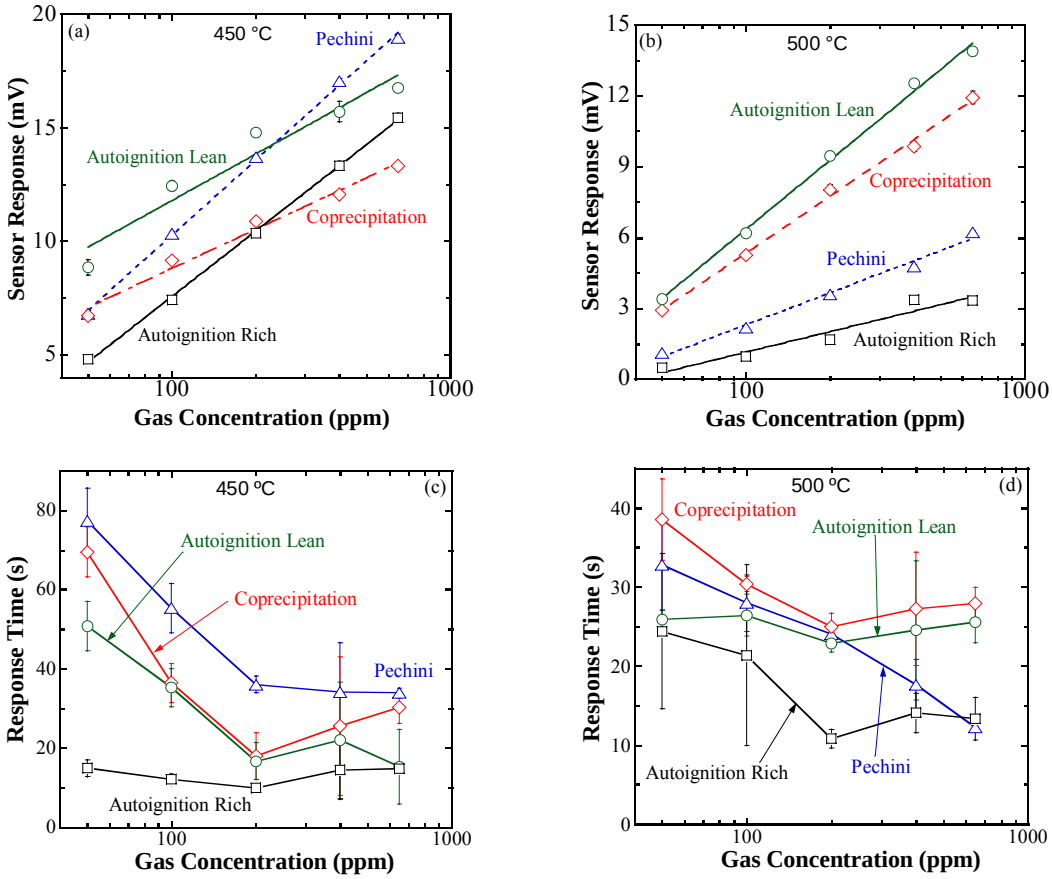

Fig. 13. Sensitivity and response time of sensors fabricated from powders prepared through different techniques (all sintered at 800 °C / 10 h). Sensitivity at (a) 450 ºC and (b) 500 ºC. Response time at (c) 450 ºC and (d) 500 ºC. The standard deviations are presented as error bars.

Fig. 13(c) and (d) show the response times for the same sensor data as presented in Fig. 13(a) and (b), respectively. The response time was calculated by taking the time required for the signal to reach 90 % of the final stable value. At 450 °C, response times ranged from 10 to 80 s and were faster at high NO concentrations. At 500 °C, the average response time decreased to a range of 10 to 40 s and the response time became relatively independent of NO concentration. At 450 °C the auto-ignition rich exhibited nearly constant response times.

Additionally, at both 400 and 500 °C the auto-ignition rich had the fastest and most stable responses of all samples.

Table 2 provides a comparison of the response time and overall sensitivity as a function of powder surface area and electrode grain size. These differences are a result of the different powder preparation techniques. Though the curves in Fig. 13(a) and (b) deviate slightly from linearity over the total gas concentration range, the overall sensitivity is determined from their slopes. At 450 °C, Pechini powders had the highest sensitivity and co-precipitation powders had the least. At 500 °C, auto-ignition lean powders had the highest sensitivity and auto-ignition rich powders had the lowest. Though these results show that microstructure plays a role in sensitivity, no direct correlation can be made between them. Further analysis of sensitivity over specific concentration regions and temperatures may elucidate a relationship.

Synthesis Technique	**Powder Surface Area[a] (m^2/g)**	**Electrode Grain Size[b] (μm)**	**Sensitivity (mV/decade)**		**Response Time[c] (s)**	
			450°C	500°C	450°C	500°C
Autoign. Rich	16.7	0.146 ± 0.055	9.59	2.88	13.2 ± 2.2	16.8 ± 5.8
Pechini	3.7	0.292 ± 0.110	10.99	4.49	47.4 ± 19.1	23.0 ± 8.2
Autoign. Lean	7.6	0.292 ± 0.100	6.81	9.70	28.0 ± 15.0	25.0 ± 6.8
Co-precipitation	9.2	0.285 ± 0.111	5.71	7.99	36.0 ± 20.0	29.8 ± 1.4

Table 2. Correlation between synthesis techniques and sensor responses.
([a] B.E.T. surface areas measured on as-calcined powders, [b] Grain size measurements of sintered electrodes from SEM micrographs, and [c] Average value of response times for five different ppm ranges, based on 90 % criteria.)

There was a direct relationship between electrode microstructure and response time. The auto-ignition fuel-rich powders had the highest surface area and resulted in the finest grained electrode microstructures and when used for fabricating sensors. These sensors had the fastest response times of all the samples for both 450 and 500 °C. The powders synthesized with the three other techniques had significantly lower surface areas. When these three types of powders were used to fabricate sensors, the electrodes had similarly-sized (grain size ~0.4 μm) microstructures. Furthermore, all three had essentially the same response time, within the

statistical significance of the data. Hence, the electrode grain size may be concluded to be directly related to response time.

In order to further investigate the effect of electrode microstructure on response time, four sensors were fabricated using the co-precipitated La_2CuO_4 powder. These sensors were sintered at four different temperatures, which resulted in microstructures as shown in Fig. 9. Their responses were measured at 500 °C, with response times determined in the same manner used earlier. As shown in Fig. 14 the sensors had a logarithmic dependence on grain size, increasing from approximately 25 s for 100 nm grained electrodes to more than 5 min for 5 μm grained electrodes. This result was not surprising since this type of dependence was observed in other studies of potentiometric and resistance-type pollutant sensors [20]. Based on these results La_2CuO_4 prepared by the auto-ignition rich method was selected for further studies. The detailed sensing properties of this sample will be presented and discussed in the following section.

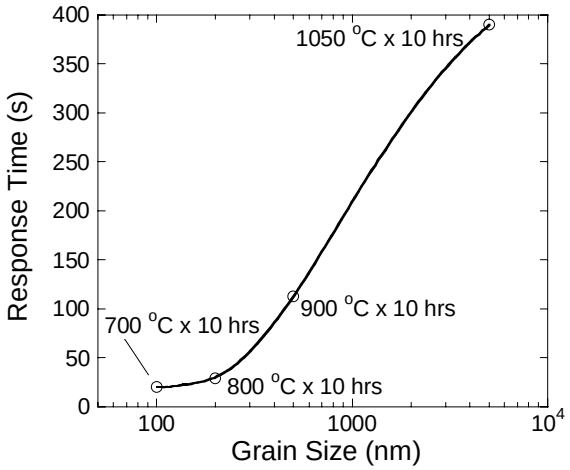

Fig. 14. Response times for potentiometric sensors operating at 500 °C and exposed to step changes in NO concentration in simulated combustion exhaust. The sensors were fabricated with La_2CuO_4 powders synthesized via co-precipitation and sintered at different isothermal dwell temperatures as indicated in graph.

4-1-4. Sensing Properties of La_2CuO_4-based Sensors

The sensor response (mV) obtained while stepping the NO concentration is plotted against time in Fig. 15(a). The NO concentration at each step is labeled in the figure. The time to reach 90 % of the steady-state EMF value (i.e., the response time) was less than 30 s for all gas

concentrations at 450 °C. As shown in Fig. 15(b), the concentration measurement of NO showed good reproducibility between different runs repeated over a 300 h period under the same conditions.

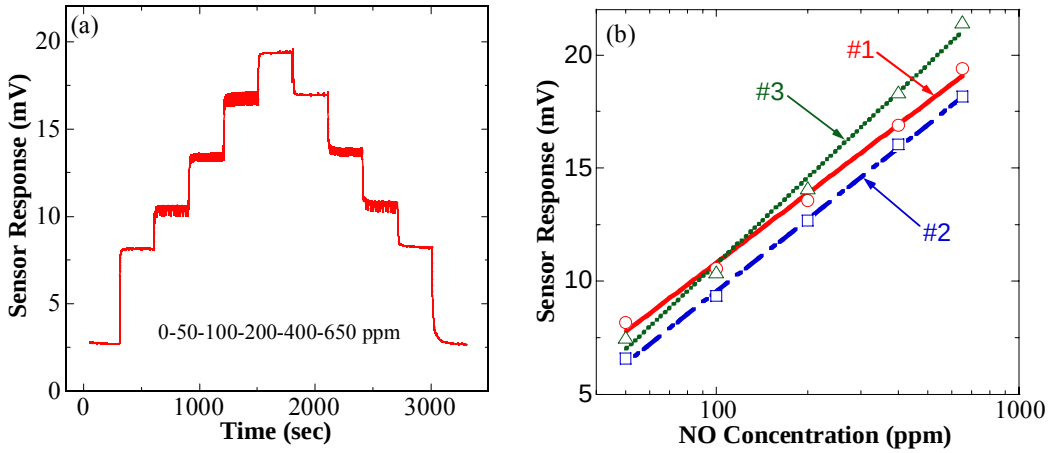

Fig. 15. Sensor response to NO (0 – 650 ppm) at 450 ºC in 3 % O_2 with N_2 balance. (a) Typical sensor response vs. steps in NO concentration, (b) Reproducibility of sensor response vs. NO concentration for different measurements under same conditions.

The relative sensor responses to varying NO, NO_2, CO, CO_2, and O_2 concentrations are plotted in Fig. 16. These sensor showed high sensitivity to NO, CO, and NO_2 at 450 ºC, whereas the cross-sensitivity to O_2 and CO_2 was negligible.

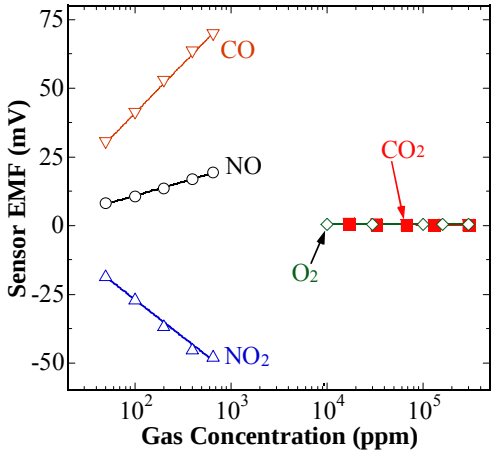

Fig. 16. La_2CuO_4 sensor response to NO, NO_2, CO, and CO_2 in 3 % O_2, and O_2 in N_2 at 450 ºC.

4-1-5. Temperature Dependence of La_2CuO_4-based Sensors

The temperature dependence of the NO response was investigated between 350 and 550 ºC As shown in Fig. 17(a), changes in the sensor EMF were very small above 500 °C and had values less than 5 mV for 650 ppm of NO. At 350 ºC and below the response was saturated.

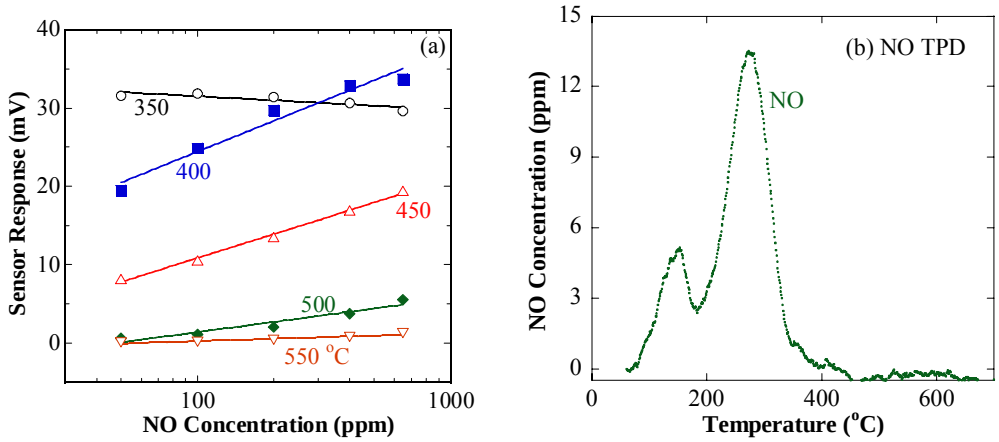

Fig. 17. Sensing and desorption behavior in the presence of NO gas. (a) Sensor response to steps in NO concentration (3 % O_2), (b) TPD of NO (1 %) over La_2CuO_4 powder.

This temperature dependence can be explained with the TPD (Fig. 17(b)) and TPR results (not shown). There were no reactions observed up to 800 °C during the TPR for either direct decomposition of NO to N_2 and O_2 or the oxidation of NO to NO_2. Therefore, any catalytic mechanism (e.g. mixed potential) can most likely be ruled out.

As clear from the TPD results in Fig. 17(b), NO does not fully desorb from the surface of La_2CuO_4 until temperatures above 400 °C. Therefore, the sensor response is unstable below 400 °C because the metal-oxide surface is saturated with adsorbed gas. That is, below 400 °C the rate of NO adsorption is greater than the rate of NO desorption. Above 400 °C, the rate of NO desorption is greater than the rate of NO adsorption, and any surface NO species are now directly proportional to the gas-phase composition. Therefore, the sensing mechanism is more likely due to adsorption of the gas and the resulting change in Fermi level of the oxide.

The temperature dependence of La_2CuO_4 was also investigated for CO. The plot of the sensor response (mV) vs. logarithm of CO concentration (ppm) was linear between 300 and 550 ºC (Fig. 18(a)). The sensitivity to CO decreased significantly above 450 °C. The TPD

results for $CO+O_2$ (Fig. 18(b)) show broad desorption of CO_2 and CO between 200 and 450 ºC. This indicates that the large CO response at temperatures below 450 °C is likely due to CO adsorption and related surface reduction.

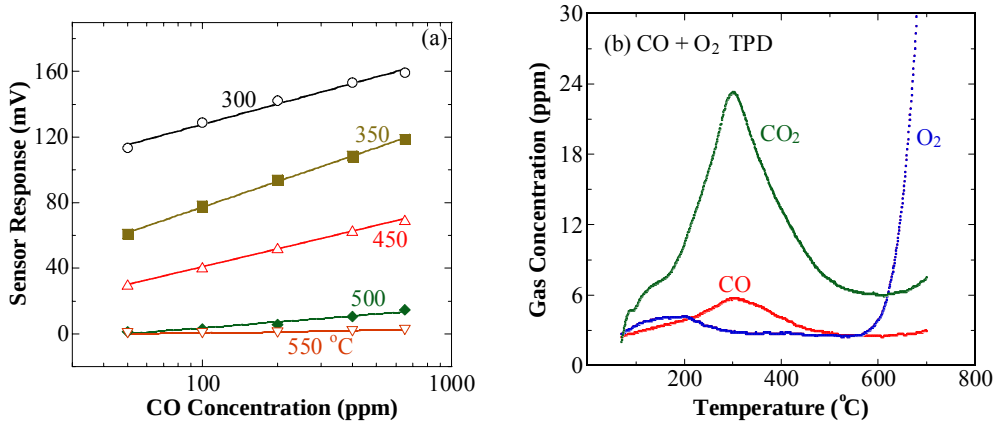

Fig. 18. Sensing and desorption behavior in the presence of CO gas. (a) Sensor response to steps in CO concentration (3 % O_2), (b) TPD of CO (500 ppm) + O_2 (1 %) over the La_2CuO_4 powder.

The NO_2 sensitivity of La_2CuO_4 as a function of temperature was also studied and was found to be more complicated then the cases for NO and CO. As presented in Fig. 19, the NO_2 response was strongly temperature-dependent and there was an abrupt decrease in sensitivity above 500 °C.

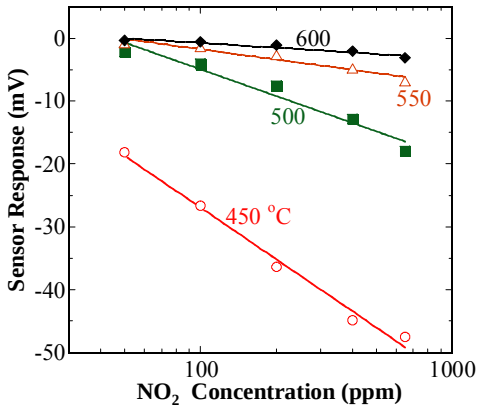

Fig. 19. Sensor response to steps in NO_2 concentration (3 % O_2).

The TPR results (Fig. 20(a)) show that NO_2 began converting to NO and O_2 above 250 °C and was completely reduced around 600 °C. Thus, the sensor response to NO_2 over this

temperature range likely involves heterogeneous catalysis. The results of the NO_2 TPD (Fig. 20(b)) also indicate that surface reactions occurred. NO_2 desorption began at 225 °C and was followed by a similar desorption peak for NO, but shifted 25 ºC higher. Additionally, the second NO desorption peak lined up with the desorption peak for chemisorbed oxygen. At temperatures above 600 °C lattice oxygen from the sample was emitted, as indicated by the increase sharp increase in O_2 desorption. Clearly, a series of complex reaction steps occur on the surface of La_2CuO_4 over the temperature range where the sensor is most sensitive to NO_2.

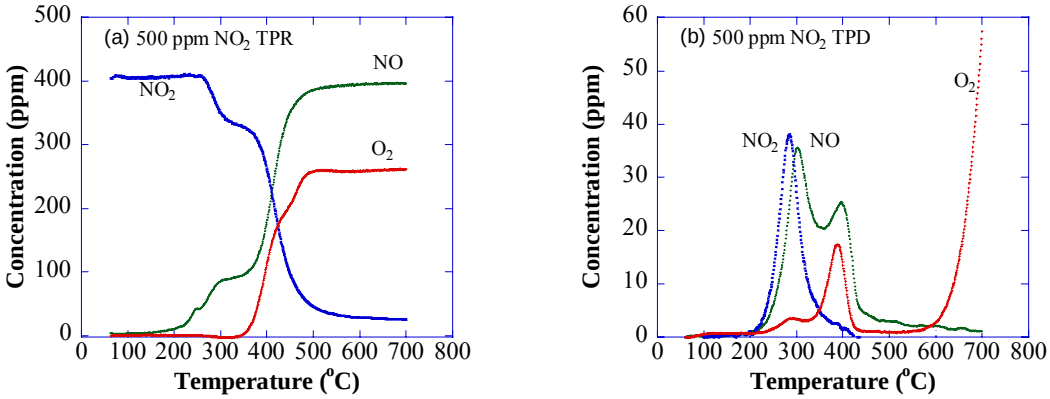

Fig. 20. TPR/TPD of NO_2 over the La_2CuO_4 powder. (a) TPR, (b) TPD of NO_2 (500 ppm).

4-1-6. Selectivity to NO

The response of the sensor to variations in NO concentration was studied in the presence of other gases. NO sensitivity was unaffected as the O_2 concentration was changed from 3 to 30 % (Fig. 21(a)). In the NO+O_2 TPD experiments, the O_2 was found to not affect NO adsorption. The TPD results (not shown) revealed NO desorption peaks very similar to those obtained in the TPD of NO (Fig. 17(b)). The addition of 3 % H_2O to NO shifted the sensor response down approximately 2 mV, but the slope remained about the same (Fig. 21(b)). The formation of a hydroxylated surface by water may influence the NO sensing behavior. Addition of CO gradually decreased the slope of the response and increased the measured EMF values (Fig. 21(c)). This is surprising since the response of the sensor is positive when exposed to both NO and CO individually. Thus, one would expect an additive response.

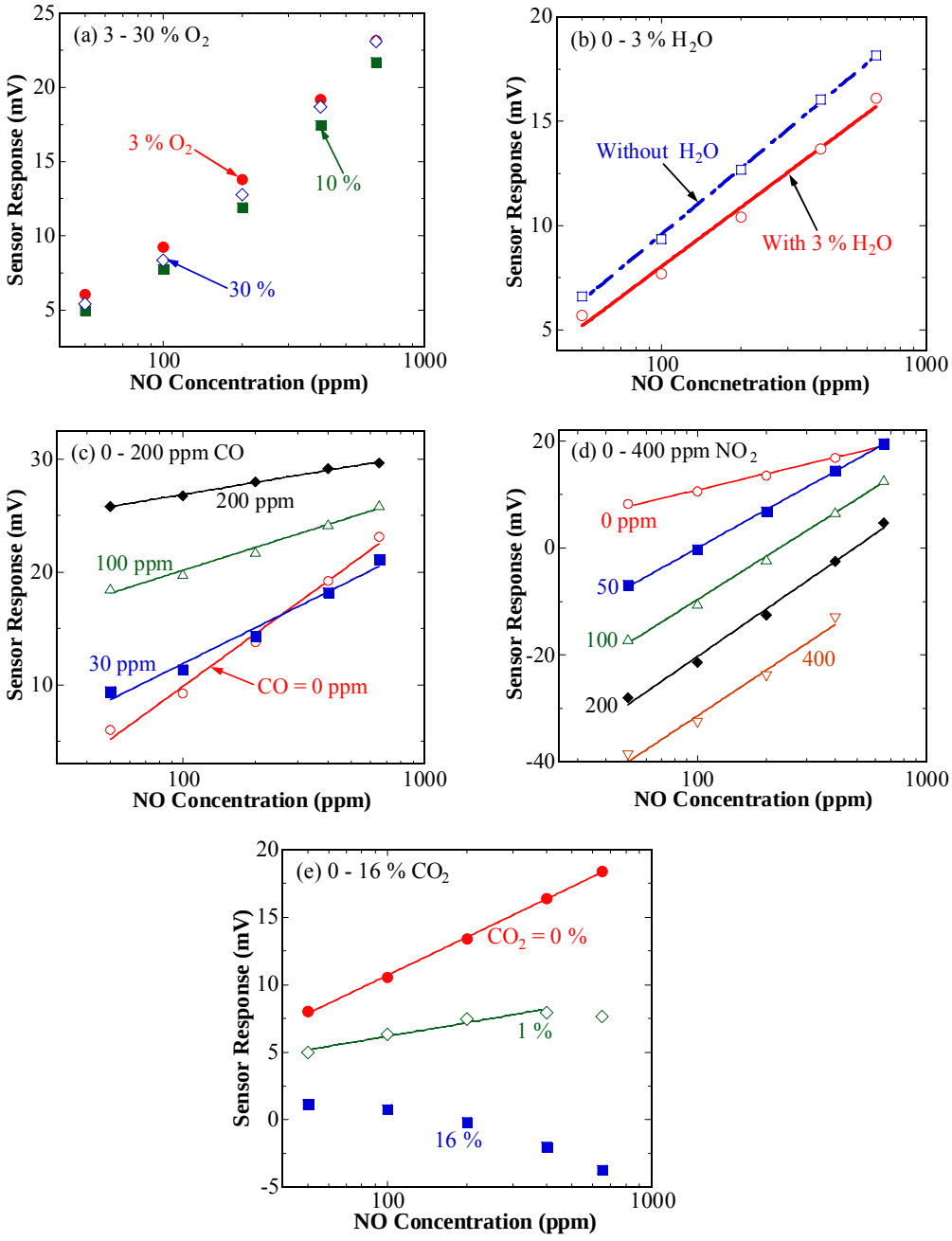

Fig. 21. Effect of O_2, H_2O, CO, NO_2, and CO_2 on the NO response at 450 ºC and in N_2. (a) O_2 effect (3 – 30 %), (b) H_2O effect (0 – 3 %), (c) CO effect (0 – 200 ppm), (d) NO_2 effect (0 – 400 ppm), (e) CO_2 effect (0 – 16 %). Measured in 3 % O_2 for (b) through (e).

Comparing the TPD of NO (Fig. 17(b)) to the TPD of NO+CO+CO_2 (Fig. 22(a)) shows that the presence of CO enhanced the NO adsorption, so that NO continued to desorb

up to 800 °C. Thus, the decrease in sensitivity with CO addition can be described in terms of the surface saturation that was exhibited below 400 ºC for the sensor response to NO alone (Fig. 17(a)). The intense CO_2 desorption peak from 200 to 500 ºC in Fig. 22(a), probably resulted from the surface reactions of CO with adsorbed oxygen or lattice oxygen. The catalytic activity of CO oxidation was high above 200 ºC, as observed during the NO+CO+O_2 TPR (Fig. 22(b)).

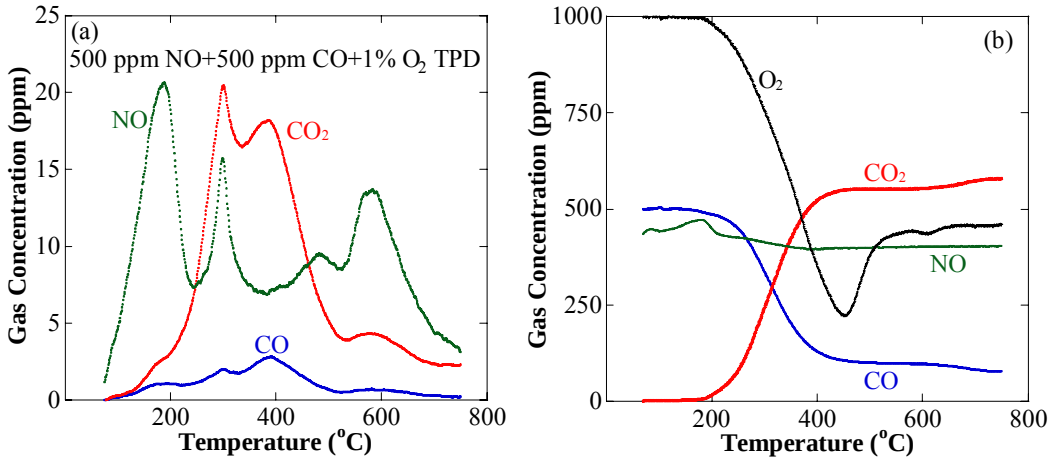

Fig. 22. TPD/TPR of NO+CO+O_2 over the La_2CuO_4 powder. (a) TPD of NO (500 ppm) + CO (500 ppm) + O_2 (1 %), (b) TPR.

The NO sensitivity of the sensor was strongly affected by NO_2 as seen in Fig. 21(d), where the baseline shift occurred with increasing NO_2 concentration. The slope remained positive even though there were large changes in the EMF values. The effect of CO_2 is presented in (Fig. 21(e)). High concentrations of CO_2 the NO response reversed and became negative in slope. The results of the NO+CO_2 TPD in Fig. 23 might help explain this phenomenon. When NO and CO_2 were co-adsorbed, the CO_2 displaced the NO adsorbates and shifted the NO desorption peaks to less than 200 ºC

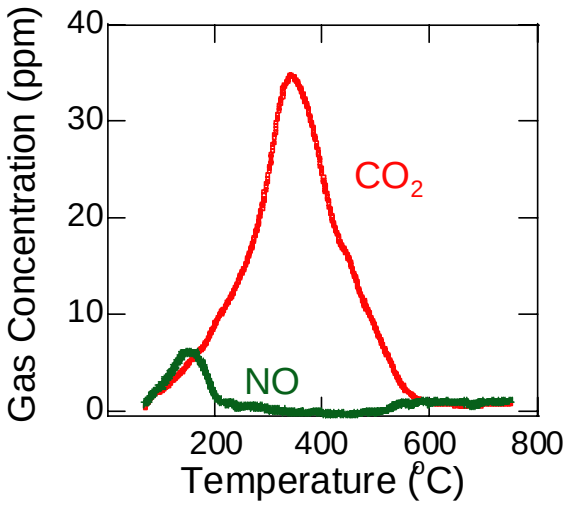

Fig. 23. TPD of NO (500 ppm) + CO_2 (1000 ppm) over the La_2CuO_4 powder.

4-2. WO_3-based Sensors

4-2-1. Characterization of WO_3 Electrodes

Fig. 24 shows a scanning electron micrograph of a WO_3 and a Platinum layer on the YSZ-8Y substrate prepared by sintering at 800 °C for 10 h. The WO_3 thick film exhibited a very porous microstructure with 0.5 to 3 μm grains and 10 to 30 μm thickness. The porous Platinum layer was deposited uniformly and had a thickness of approximately 9 μm.

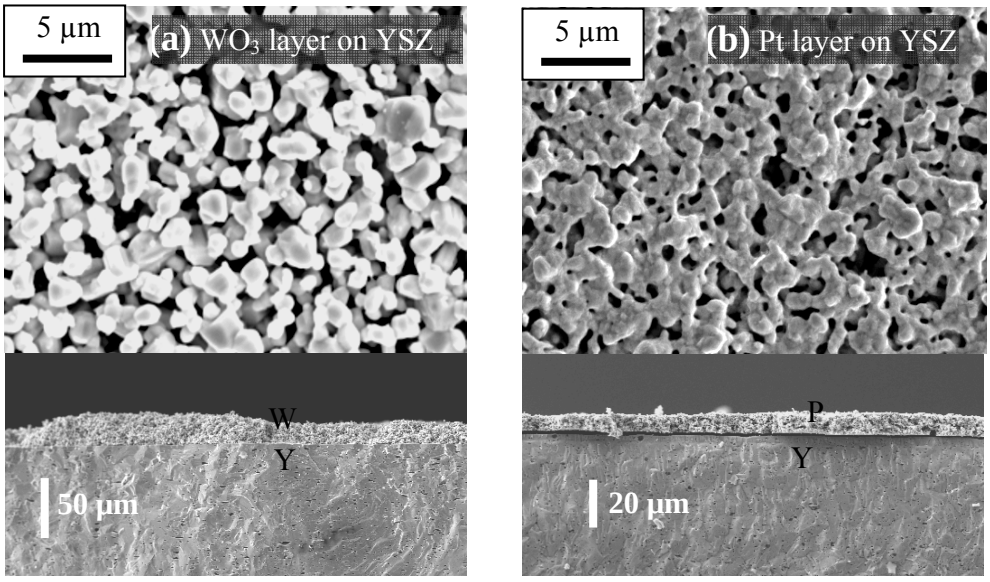

Fig. 24.Scanning electron micrograph of the (a) WO_3 and (b) Pt layers of the sensor electrode.

4-2-2. Sensing Properties

The WO_3 sensor response is plotted against time in Fig. 25 for increasing steps in concentration of NO (50 – 650 ppm) and NO_2 (10 – 200 ppm) at 650 °C in 3 % O_2. The response was positive for NO_2 and negative for NO. The direction of the response for the n-type WO_3 is opposite that of p-type La_2CuO_4. This agrees with previous results, where the potentiometric sensor measurements were performed with different cell configurations [14, 15]. Values of the sensor EMF measured for NO_2 were much higher than those formerly reported at 650 °C in air. For example, the EMF measured for 200 ppm NO_2 was approximately 90 mV in these experiments, which is more than two times higher than in the results from the literature.

The response time of the sensor was dependent on the gas concentration, showing faster responses at higher concentration for both NO and NO_2. The response time was approximately 20 s at higher concentrations (400 – 650 ppm) and 50 s at lower concentrations (50 – 100 ppm) of NO. The sensor response to NO_2 was faster than that of NO for low concentration (10 – 200 ppm) values. The response time was less than 15 s for 10 to 20 ppm NO_2 and the sensor attained a steady-state value within 60 s at 650 °C.

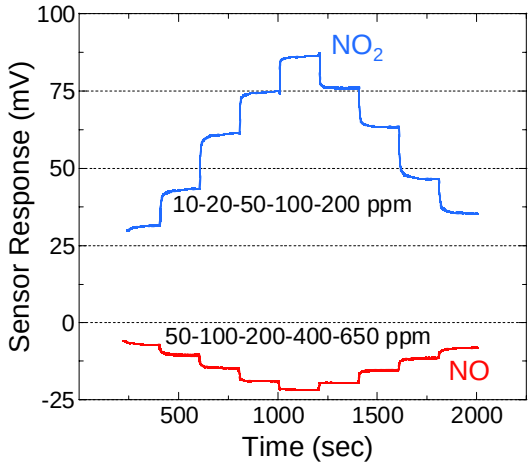

Fig. 25. Typical plot of sensor EMF (mV) vs. time (sec) as a function of NO (50 – 650 ppm) and NO_2 (10 – 200 ppm) concentration steps at 650 ºC in 3 % O_2 and balance N_2.

The sensor EMF values for a particular gas step for increasing NO_x concentrations were slightly different than those measured during decreasing concentration steps at 650 °C. These differences were more pronounced at lower gas concentrations for both NO and NO_2. This gas history effect decreased with increasing temperature and became negligible above 700 °C for

both NO and NO_2, indicating that the kinetics of adsorption and desorption might be dissimilar at lower temperatures. The aforementioned WO_3 measurements were repeated several times over 200 h. The sensor EMF values were repeatable with less than 10 % difference and no systematic trends were observed for the recurring sensor measurements. An average of the EMF values measured for increasing and decreasing concentration was used for further analysis.

4-2-3. Temperature Dependence of WO_3-based Sensors

The temperature dependence of the NO_x sensor response was investigated between 550 and 800 °C. The sensor response (mV) vs. logarithm of NO concentration (ppm) is linear between 600 and 750 °C for 50 to 650 ppm of NO (Fig. 26(a)). The slope decreased gradually with increasing temperature from 600 to 700 °C and decreased abruptly at 750 °C. The general tendency of the temperature dependence was in agreement with previous results obtained by using a half-open YSZ tube [14].

The temperature dependence of NO_2 sensitivity was also studied, as presented in Fig. 26(b). A linear relationship was observed between 550 and 800 °C for 10 to 200 ppm of NO_2. The slope increased slightly from 550 to 700 °C, with a sudden decrease at higher temperatures. This was somewhat different from the previous observation showing an abrupt decrease in the slope at 700 °C [14].

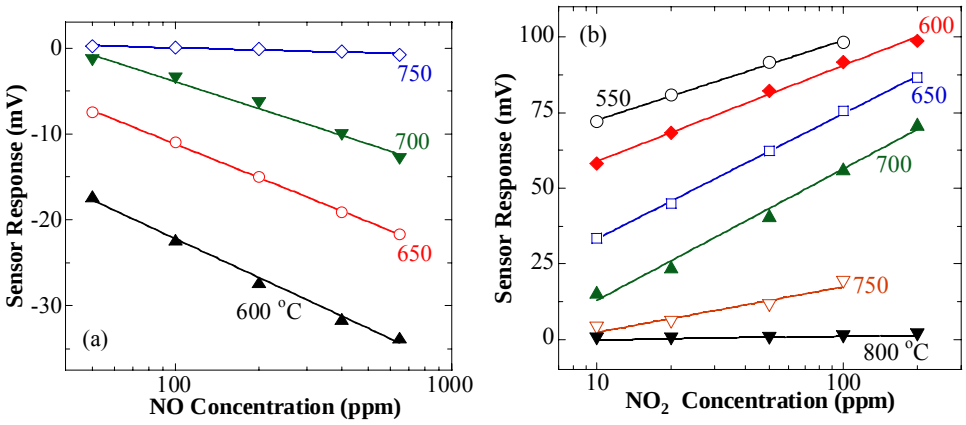

Fig. 26. Variation of the NO_x sensitivity as a function of temperature in 3 % O_2. (a) NO from 600 to 750 ºC, (b) NO_2 from 550 to 800 ºC.

As found for the La_2CuO_4-based sensor (Fig. 17), the sensor response decreased with increasing operating temperature [21, 22]. This is due in part to a decrease in the amount of adsorbed gas on the surface of the semiconductor with increasing temperature, which occurs as the rate of gas desorption becomes faster than that of adsorption [5]. In addition, a dissymmetry of the catalytic activity between the two electrodes might also explain these results. TPR experiments of the catalytic activity of a Pt electrode for the reduction of NO_2 was found to be higher than that of WO_3 (Fig. 27). The difference in the activity became smaller as temperature was increased, which would explain the reduced sensor response.

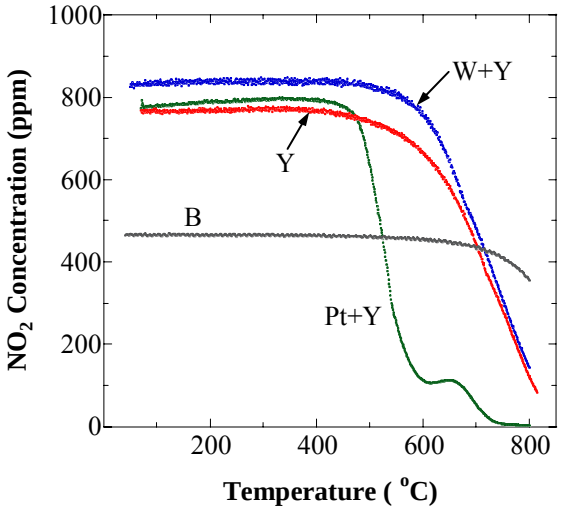

Fig. 27. TPR of NO_2 over WO_3 on YSZ (W+Y), Pt on YSZ (Pt+Y), YSZ (Y), and blank (B).

4-2-4. Selectivity to NO

The effect of H_2O, NO_2, CO, CO_2, and O_2 on NO sensitivity was investigated at 650 °C. The WO_3-based sensor was able to selectively detect NO in the presence of CO_2 (Fig. 28(a)). The sensor EMF values were very close to each other for three different concentrations of CO_2, with a maximum difference of less than 1.5 mV. The sensor was also selective to NO without any interference from variations of 3 to 30 % O_2 concentration (Fig. 28 (b)).

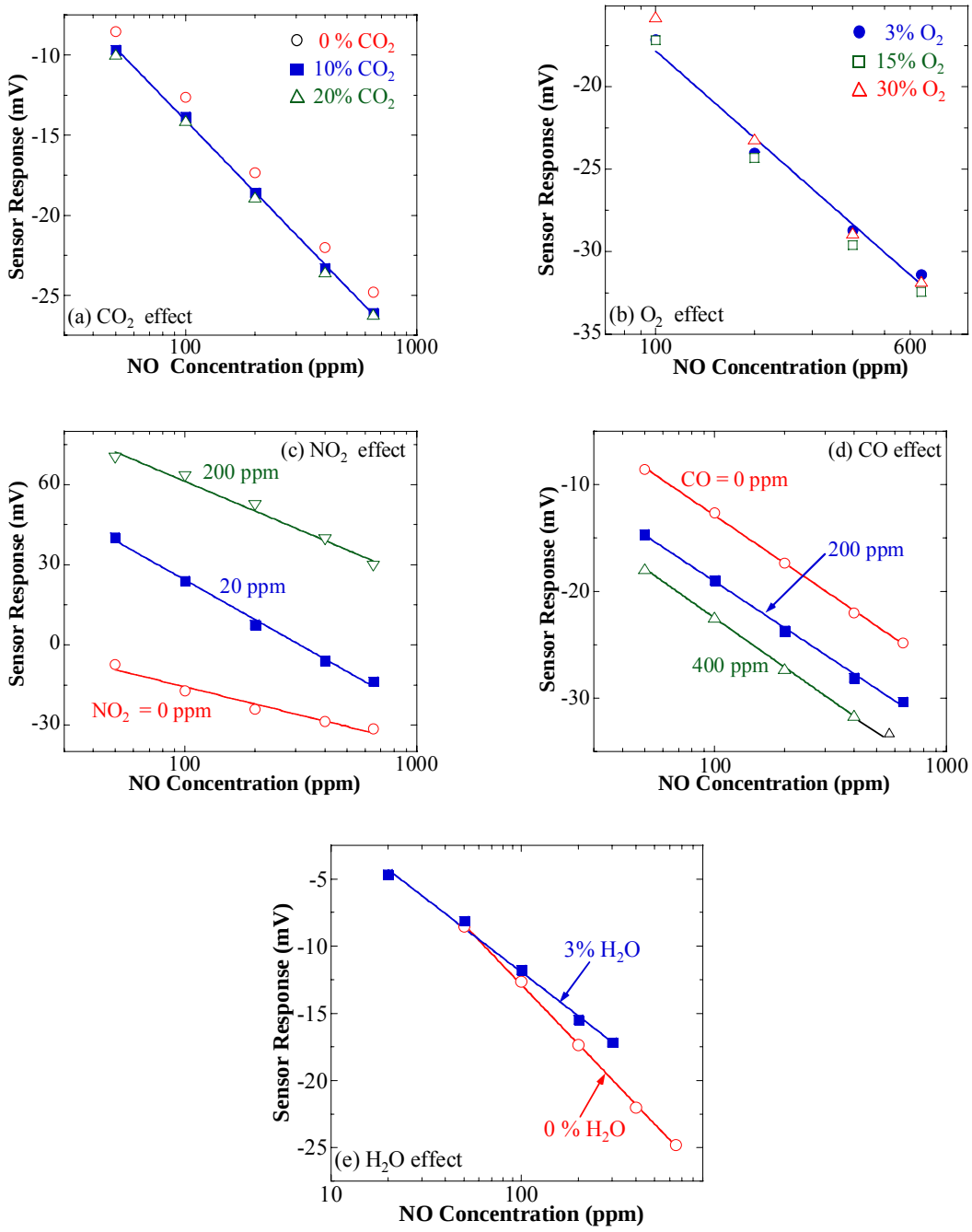

Fig. 28. Effect of CO_2, O_2, NO_2, CO, and H_2O on the NO response at 650 ºC and in N_2 balance. (a) CO_2 effect (0 – 20 %), (b) O_2 effect (3 – 30 %), (c) NO_2 effect (0 – 200 ppm), (d) CO effect (0 – 400 ppm), (e) H_2O effect (0 – 3 %). Measured in 3 % O_2 for (a) and (c) through (e).

The influence of NO_2 on the NO sensitivity is shown in Fig. 28(c). When NO_2 was added to the NO step, the EMF values increased significantly but the sign of the slope remained the same. The slope increased considerably with the addition of 20 ppm NO_2. The gas-phase oxidation of NO in reaction (1) is thermodynamically favorable in these conditions, and thus at equilibrium most of the NO should be converted to NO_2.

$$NO + 1/2O_2 \rightarrow NO_2 \quad (1)$$

However, conversion of NO to NO_2 was not observed in the TPR experiments (Fig. 29). This is most likely due to unfavorable NO oxidation kinetics. As with the La_2CuO_4-based sensor, the mixed potential theory cannot explain the occurrence of the NO sensitivity of the WO_3-based sensor.

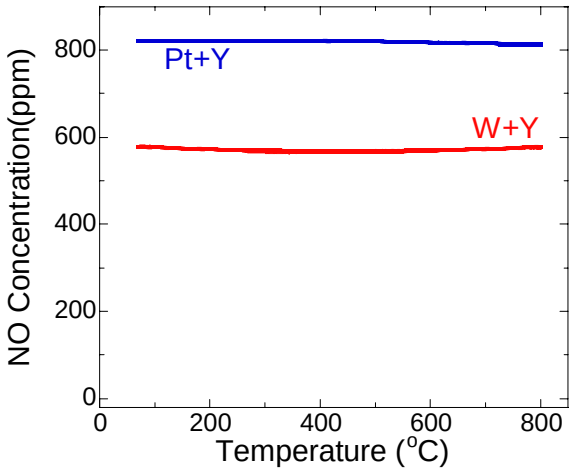

Fig. 29. TPR of $NO+O_2$ (1000 ppm) over WO_3 on YSZ (W+Y) and Pt on YSZ (Pt+Y).

Fig. 28(d) shows the effect of CO on the NO sensor response. The EMF values increased without any significant change in slope. In TPR experiments (Fig. 30) WO_3 and Pt electrodes exhibited different catalytic activities for the oxidation of CO at 650 °C. Therefore, the reaction can take place either non-electrochemically as in (2) or electrochemically as in (3).

$$CO + \frac{1}{2}O_2 \rightarrow CO_2 \quad (2)$$

$$CO + O^{2-}(lattice) \rightarrow CO_2 + 2e^- \quad (3)$$

This difference in catalytic activity might give rise to the CO response. However, neither CO_2 formation from the reaction of NO with CO in (4) nor the oxidation of NO in (1) was observed in this system.

$$CO + NO \rightarrow CO_2 + \frac{1}{2} N_2 \tag{4}$$

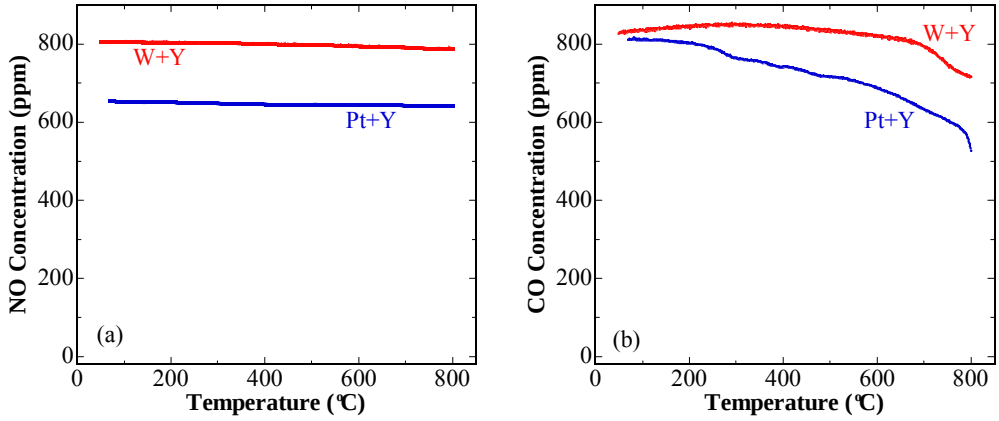

Fig. 30. TPR of NO+CO+O_2 (1000 ppm) over WO_3 on YSZ (W+Y) and Pt on YSZ (Pt+Y). (a) NO concentration, (b) CO concentration.

As shown in Fig. 28(e), the slope decreased slightly by addition of 3 % H_2O. This is most likely a result of the formation of a hydroxylated surface, where OH^- are bonded to the metal cations and H^+ bond to the anions of the metal oxide [5]. A linear relationship was still shown even in the presence of H_2O.

4-2-5. Selectivity to NO_2

The influence of CO_2 (0 – 20 %) and H_2O (0 – 3 %) on the NO_2 response at 650 °C is presented in Fig. 31(a) and (b), respectively. The difference in EMF values, with and without CO_2 and H_2O, was less than 1 mV over the entire NO_2 concentration range.

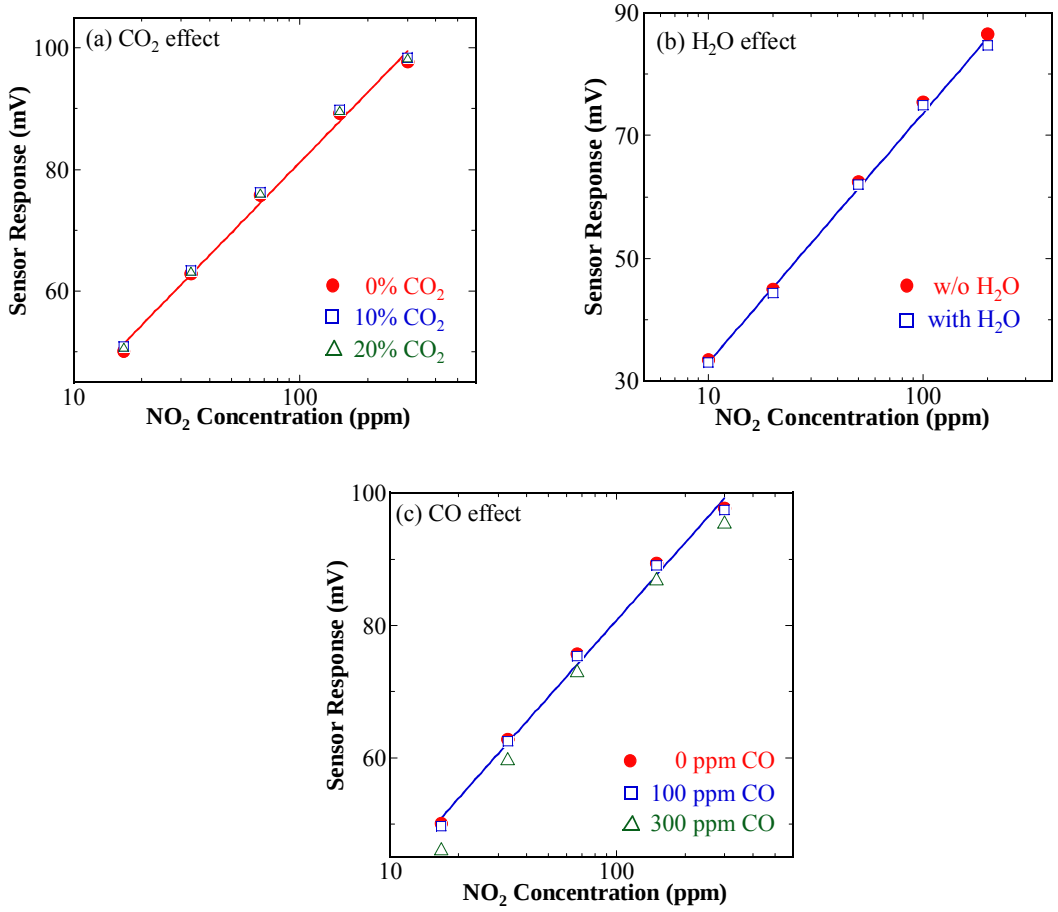

Fig. 31. Effect of CO_2, H_2O, and CO on the NO_2 response of a WO_3-based sensor at 650 ºC in 3 % O_2. (a) CO_2 effect (0 – 20 %), (b) H_2O effect (0 – 3 %), (c) CO effect (0 – 300 ppm).

As shown in Fig. 31(c), the addition of 100 and 300 ppm CO did not influence the NO_2 sensitivity. Any difference in the EMF values was still within the general range of reproducibility. As previously mentioned, the selective detection of NO over NO_2 and CO was not obtained for the WO_3 sensor, but interestingly the NO_2 response was not strongly influenced by CO. In the NO_2+CO+O_2 TPR experiments (Fig. 32), the addition of CO did not

affect the measured NO_2 concentration obtained with Pt+Y. However, the NO_2 concentration for the W+Y slightly decreased at 650 ºC, which could account for the small decrease in the EMF values (Fig. 31(c)) seen for increasing amounts of CO. Therefore, at 650 ºC NO_2 reduction reactions (5) or (6) were likely dominant over reactions (3) and (4) involving CO.

$$NO_2 \rightarrow NO + 1/2O_2 \quad (5)$$

$$NO_2 + 2e^- \rightarrow NO + O^{2-}_{(lattice)} \quad (6)$$

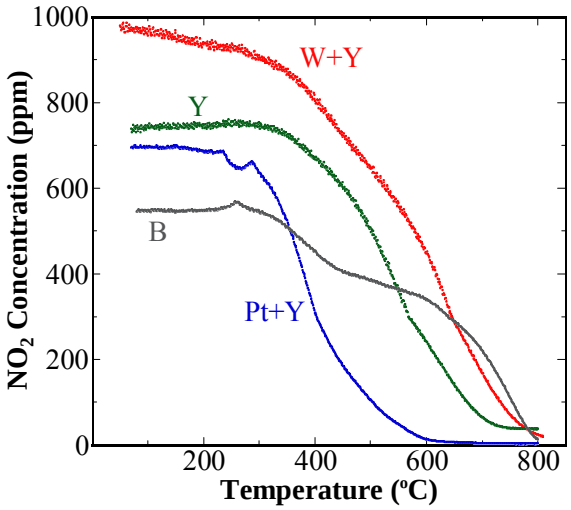

Fig. 32. TPR of NO_2+CO+O_2 (1000 ppm) over WO_3 on YSZ (W+Y), Pt on YSZ (Pt+Y), YSZ (Y), and blank (B).

The sensor consisting of WO_3 and Pt electrodes on YSZ-8Y has been demonstrated as a good candidate for the NO_2 monitoring. This sensor selectively detected NO_2 against CO, CO_2, and H_2O with very high sensitivity down to NO_2 concentrations on the order of 10 ppm.

4-2-6. Sensing Properties of WO_3-based Sensors in Simulated Exhaust

The WO_3 sensor response to NO_x (10 – 650 ppm) was tested in 3 % O_2 and in simulated exhaust conditions (3 % O_2, 3 % H_2O, 16 % CO_2, and 100 ppm CO) at 650 °C. The sensor EMF values for NO were significantly different for each case, with a much greater slope for the sensor response in the simulated exhaust (Fig. 33(a)). This higher sensitivity to NO for combustion gas compared to the 3 % O_2/N_2 mixture indicates that a complex equilibrium occurred on the electrode surface when all gas species were present. In contrast to the results

for NO, the EMF values for the NO_2 steps in the simulated exhaust were less than those in the 3 % O_2/N_2 mixture (Fig. 33(b)).

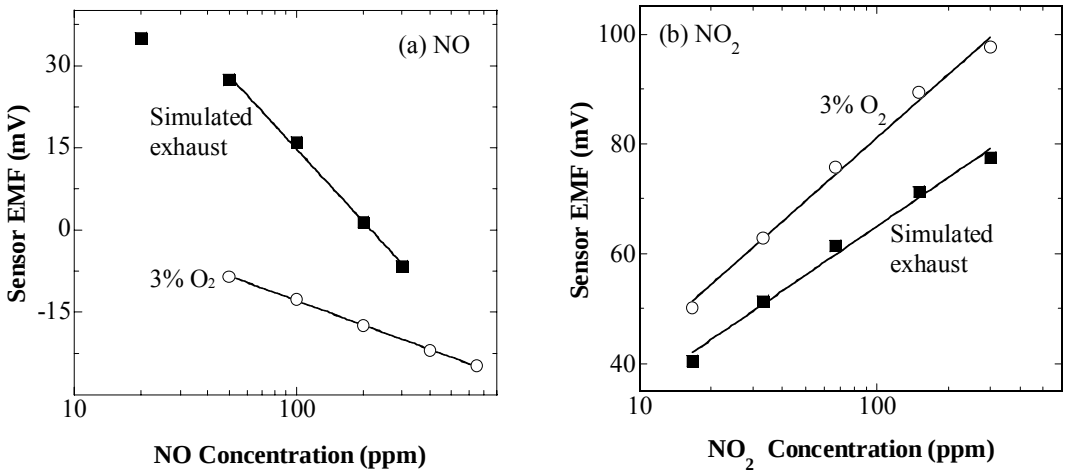

Fig. 33. Comparison of the NO_x sensitivity at 650 ºC in 3 % O_2 and in a simulated exhaust gas (3 % O_2, 3 % H_2O, 16 % CO_2, and 100 ppm CO). (a) NO and (b) NO_2 steps.

4-2-7. Selectivity to NO in Simulated Exhaust

The influence of each of the individual gases (H_2O, O_2, CO, and CO_2) on the NO_x response in simulated exhaust was investigated. For example, to study the effect of O_2, measurements were performed in varying O_2 concentrations (0.5 – 20 %) while maintaining constant concentrations of the other gases (3 % H_2O, 16 % CO_2, and 100 ppm CO). The effect of H_2O (0 – 3 %), CO_2 (0 – 16 %), and CO (0 – 200 ppm) were studied in a similar manner.

As presented in Fig. 34, the NO sensing behavior in simulated exhaust conditions was strongly affected by H_2O, O_2, and CO, but not by CO_2. The effect of H_2O in the combustion gas mixture was most noticeable (Fig. 34(a)). The difference between 0 % and 3 % H_2O in the simulated exhaust caused the sensor EMF to increase by more than 40 mV. Furthermore, the NO sensitivity increased significantly in the combustion mixture, whereas it decreased moderately in the simple O_2/N_2 based gas mixture (Fig. 28(e)).

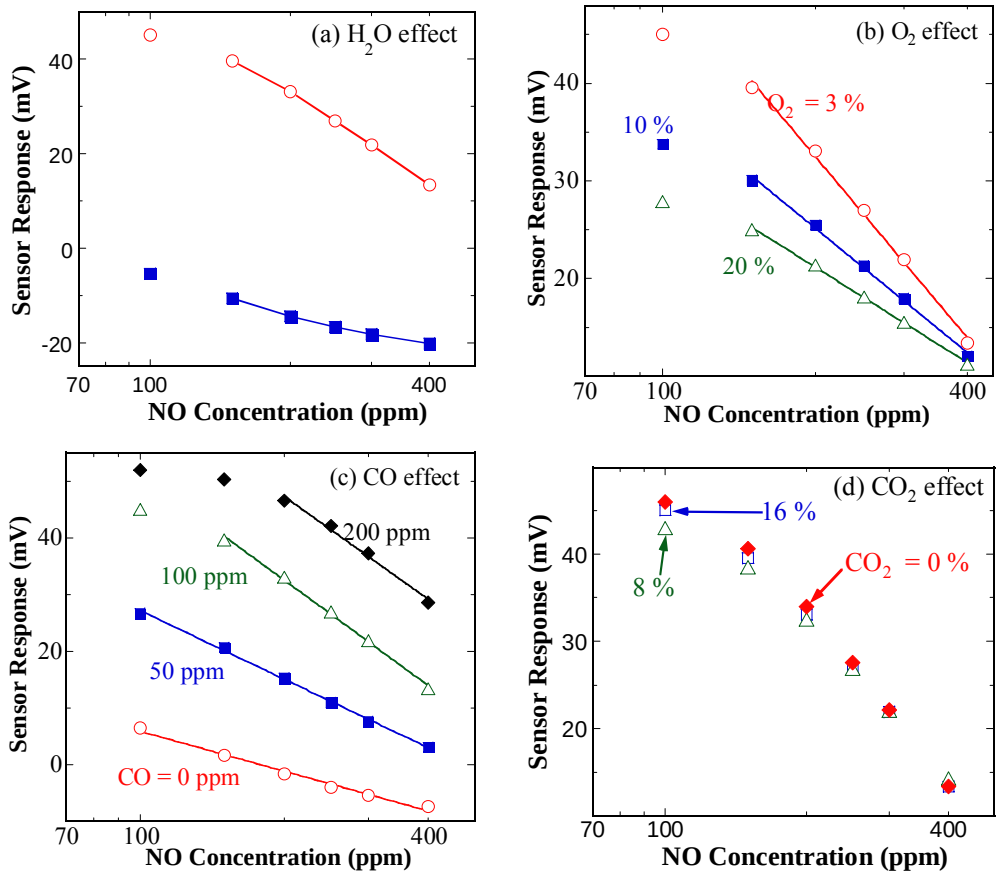

Fig. 34. Effect of H_2O, O_2, CO, and CO_2 on the NO response at 650 ºC and in a simulated exhaust gas (3 % O_2, 3 % H_2O, 16 % CO_2, and 100 ppm CO). (a) H_2O effect (0 – 3 %), (b) O_2 effect (3 – 20 %), (c) CO effect (0 – 200 ppm), (d) CO_2 effect (0 – 16 %).

In the simulated exhaust conditions, the large change in sensor response when water vapor is present on the electrode surface might enhance the kinetics of NO_2 production such as in reactions (1). On the other hand, the water vapor might result in the formation of complex NO/H_2O surface species as in reaction (7) [5,23].

$$NO + H_2O \rightarrow NO_2 + H_2 \qquad (7)$$

Fig. 34(b) shows the effect of O_2 on NO sensitivity. Increasing the concentration of O_2 caused both the EMF values and the response slope of the sensor to decrease. This was different from the case of the simple O_2/N_2 mixture, where there was no discernable O_2 effect (Fig. 28(b)). CO also had a significant influence on NO sensitivity in the simulated exhaust conditions (Fig. 34(c)). The slope of the sensor response increased as CO was varied from 0 to

200 ppm. The EMF values increased with larger CO concentrations, which is opposite the trend obtained in 3 % O_2 (Fig. 28(d)). As in the case of the simple O_2/N_2 mixture (Fig. 28(a)), the NO response in simulated exhaust conditions was relatively unaffected when CO_2 concentration was changed from 0 to 16 %.

4-2-8. Selectivity to NO_2 in Simulated Exhaust

The effects of O_2 and H_2O on the NO_2 response in simulated exhaust conditions were investigated at 650 °C. The EMF values for NO_2 decreased with increasing O_2 concentration (Fig. 35(a)). A small increase in the slope of the response occurred for an O_2 concentration of 0.5 %, but no clear changes were seen for 3 to 20 % O_2. The addition of 3 % H_2O decreased the slope with reduced EMF values (Fig. 35(b)). Interestingly, the plot obtained without 3 % H_2O in simulated exhaust was very similar to that in 3 % O_2 (Fig. 31(b)). This implies that H_2O played an important role in the NO_2 sensitivity. Neither CO (0 – 200 ppm) nor CO_2 (0 – 16 %) had a significant effect on the sensing of NO_2 in simulated exhaust (Fig. 35(c) and (d)).

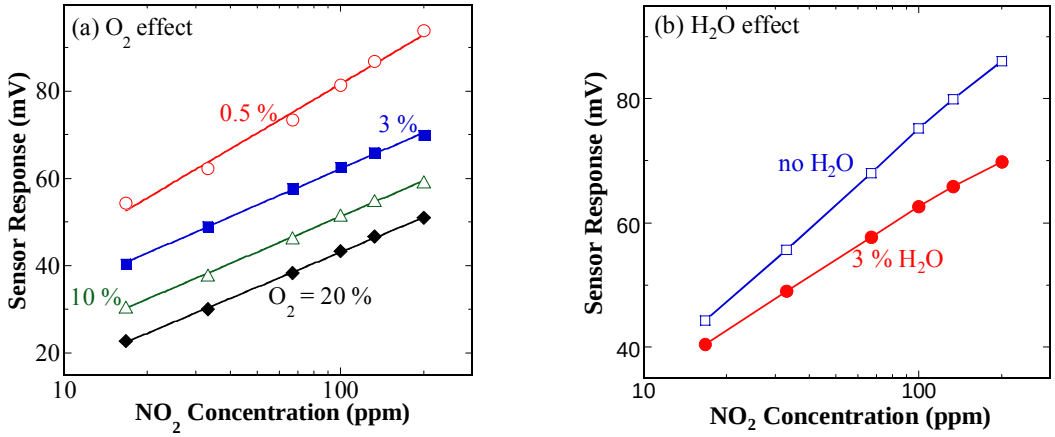

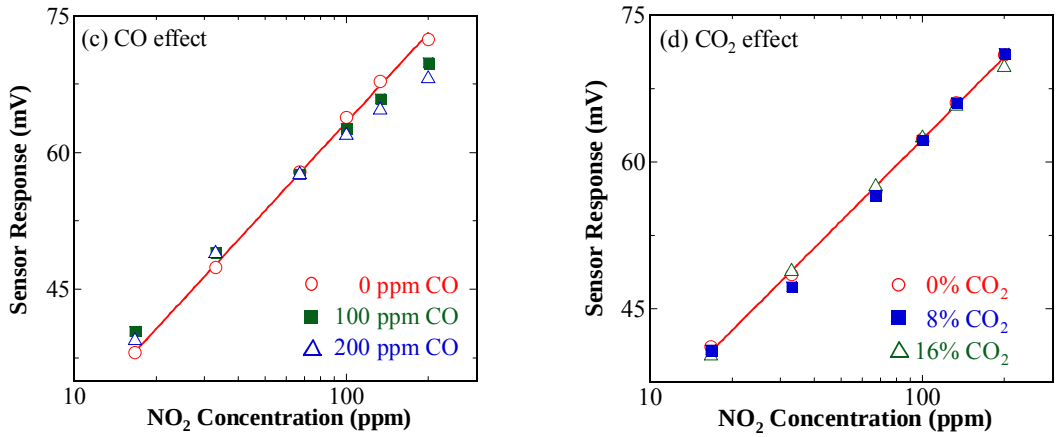

Fig. 35. Effect of O_2, H_2O, CO, and CO_2 on the NO_2 response at 650 ºC and in a simulated exhaust gas. (a) O_2 effect (0.5 – 20 %), (b) H_2O effect (0 – 3 %), (c) CO effect (0 – 200 ppm), (d) CO_2 effect (0 – 16 %).

4-3. Cr_2O_3, SnO_2, CeO_2-based Sensors

4-3.1 Characterization of Electrodes

The Cr_2O_3, SnO_2, and CeO_2 electrodes were characterized using scanning electron microscopy (SEM). SEM micrographs of the electrode surfaces are found in Fig. 36 and cross-sections between the thick films and YSZ are presented in Fig. 37. The samples were prepared by sintering at 800 ºC for 10 hr.

The Cr_2O_3 layer exhibited a porous microstructure with 0.2 to 1 μm grains (Fig. 36(a)) and 3 to 4 μm thickness (Fig. 37(a)). Grains in the SnO_2 and CeO_2 films were generally agglomerated and not well defined, with a dispersed grain size distribution (0.1 – 2 μm). Both the SnO_2 and CeO_2 were very porous (Fig. 36(b) and (c)) and between 3 and 4 μm thick (Fig. 37(b) and (c)). The porous Pt layer was deposited uniformly with a thickness of approximately 9 μm.

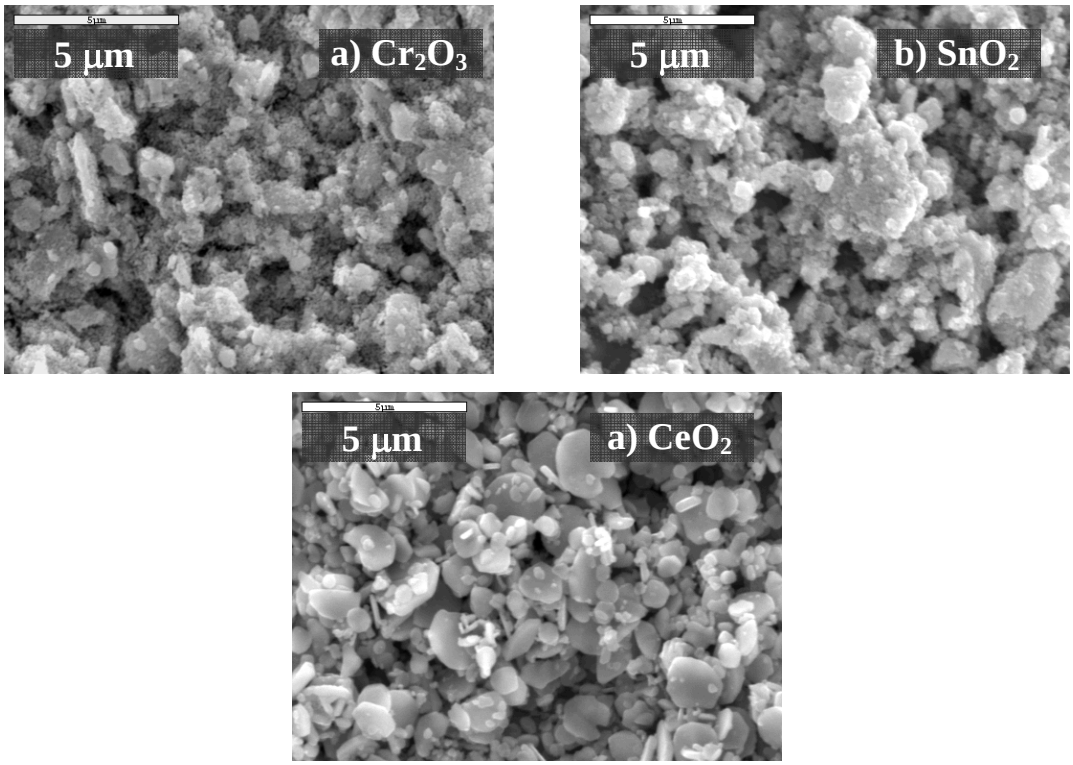

Fig. 36. Scanning electron micrograph of metal oxide electrode surface. (a) Cr_2O_3, (b) SnO_2, and (c) CeO_2.

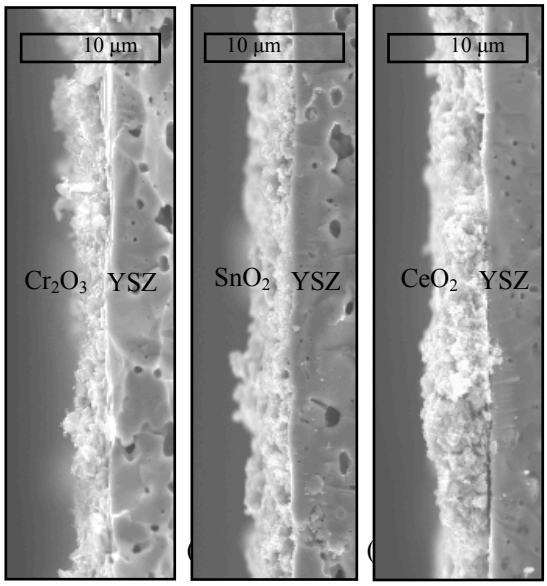

Fig. 37. Scanning electron micrograph of cross section between metal oxide and YSZ. (a) Cr_2O_3, (b) SnO_2, and (c) CeO_2.

4-3.2 Sensing Properties

Cr_2O_3-based Sensors

The response of the Cr_2O_3-based sensor is plotted against time for 9 to 230 ppm NO_2 concentration steps in 21 % O_2 (N_2 balance) from 450 to 700 ºC (Fig. 38(a)). The EMF values (mV) were positive and increased with NO_2 concentration. A positive NO_2 response was also observed during the sensor experiments performed using a WO_3-based potentiometric sensor with the same cell configuration in 3 to 21 % O_2 [24]. However, the Cr_2O_3-based sensor was less sensitive to NO_2. For example, the WO_3 sensor had a NO_2 response (Fig. 26(b)) that was about three times higher than the Cr_2O_3 response at 650 °C (Fig. 38(b)).

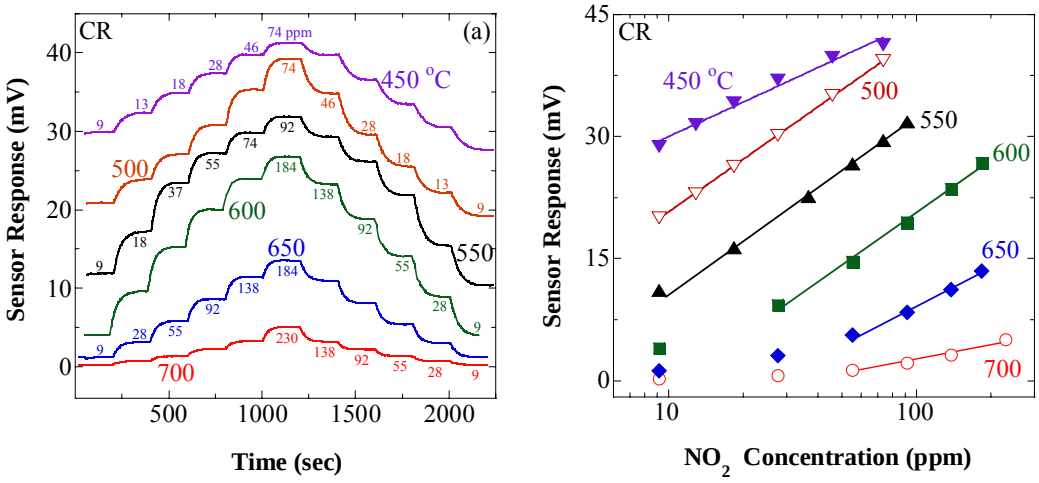

Fig. 38.NO_2 sensitivity of Cr_2O_3-based sensor (CR) in 21 % O_2 and balance N_2 at 450 to 700 ºC. (a) Plots of sensor response vs. time. NO_2 concentrations are shown for each step in ppm and (b) Plots of sensor response vs. NO_2 concentration. The lines drawn in (b) are logarithmic fits.

The response time of the Cr_2O_3 sensor did not appear to be temperature dependent between 450 and 700 ºC and the steady-state was always achieved within 150 sec (Fig. 38(a)). The sensor response was faster for increasing steps in NO_2 concentration when compared to decreasing steps. This agrees with previous results obtained with kinetics calculations assuming first order adsorption and desorption reactions. These calculations indicate that the response (from a balance gas to a sensed gas) is always faster than the recovery (from a sensed gas to a balance gas) [25]. Additionally, the EMF values were slightly larger for increasing concentration steps. This difference became more significant at lower temperatures, while it

decreases with increasing temperature and becomes negligible above 650 ºC. This is likely due to dissimilar kinetics between adsorption and desorption at lower temperatures.

The optimal operating temperature for the Cr_2O_3-based sensor is 600 °C when considering the NO_2 sensitivity and the relative kinetics of adsorption and desorption. Therefore, NO_2 selectivity experiments were performed at 600 ºC. An average of the EMF values measured with increasing and decreasing concentration was used for the following selectivity analysis. Plots of the sensor response (mV) vs. the logarithm of NO_2 concentration (ppm) are presented in Fig. 38(b). A linear relationship was observed between 450 and 600 ºC for NO_2 concentrations larger than 30 ppm. The slopes obtained from 500 to 600 ºC are comparable to each other. However, above 600 ºC the slope decreased with increasing temperature.

The NO_2 sensitivity of the Cr_2O_3 sensor at 600 ºC had good reproducibility between different measurements repeated over 11 days under the same condition (21 % O_2), as shown in Fig. 39. The slopes of the responses are similar to each other, and any differences in the EMF values at a given concentration step were as small as 0.1 to 1.5 mV. This type of reproducibility was also observed over 10 days for the SnO_2 and CeO_2 sensors (not shown).

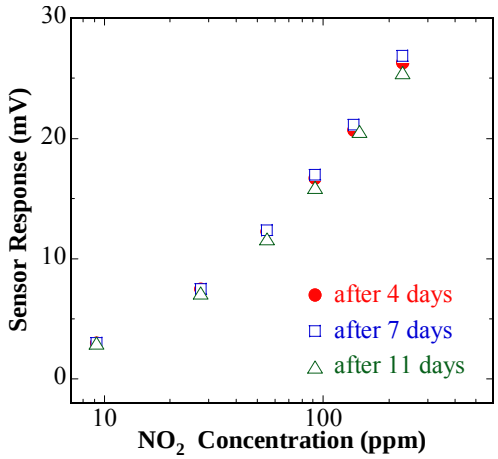

Fig. 39. Reproducibility of Cr_2O_3 sensor NO_2 sensitivity repeated over 11 days under the same condition (in 21 % O_2 at 600 ºC).

During these experiments, at least three different sensors of the same design were fabricated and tested for comparison. The EMF values measured in NO_x agreed within 10 to

20 % difference on average under the same conditions. As mentioned in previous sections, the response of each sensor was expected to be slightly different for each sensor because variations in fabrication may lead to differences in parameters important to sensitivity [26]. This demonstrates the importance of accurate control of fabrication conditions.

SnO_2-based Sensors

The NO_2 sensing response of the SnO_2-based sensor between 500 and 700 ºC is presented in Fig. 40. The NO_2 response for this sensor had positive slopes and EMF values, just as with the Cr_2O_3- and WO_3-based sensors [24].

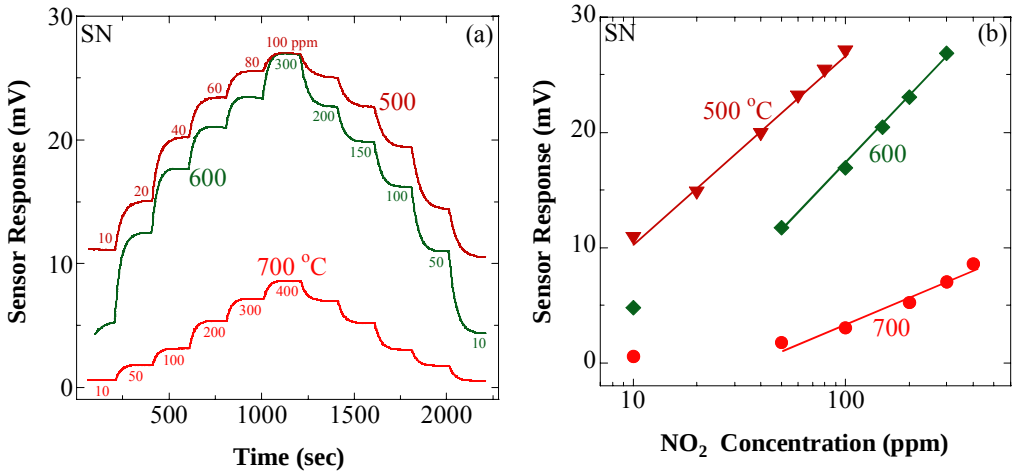

Fig. 40. NO_2 sensitivity of SnO_2-based sensor (SN) in 21 % O_2 and balance N_2 from 500 to 700 ºC. (a) Plots of sensor emf vs. time. NO_2 concentrations are shown for each step in ppm and (b) Plots of sensor emf vs. NO_2 concentration. The lines drawn in (b) are logarithmic fits.

The time required to reach 90 % of a steady-state value (i.e., the response time) for the SnO_2 sensor is less than 100 sec between 500 and 700 ºC (Fig. 40(a)). As with the Cr_2O_3 sensor, the response time was faster when the NO_2 concentration was increased rather than decreased. An average of the sensor EMF values measured with increasing and decreasing concentrations was used in constructing sensitivity plots (Fig. 40(b)). A linear relationship was observed between 500 and 700 ºC for NO_2 concentrations larger than 50 ppm. The response with the largest slope occurred at 600 ºC.

CeO_2-based Sensors

The NO_2 sensing behavior of the CeO_2-based sensor was very similar to the Cr_2O_3 and the SnO_2 sensor (Fig. 41(a)). This includes the direction of response, temperature effect on sensitivity, and the response times. There was a decrease in the slope of the sensor response for temperatures above 600 ºC (Fig. 41(b)). The response time of the CeO_2 sensor was about 15 s faster for increasing rather than decreasing NO_2 concentration. The sensor response began to saturate below 550 ºC (not shown).

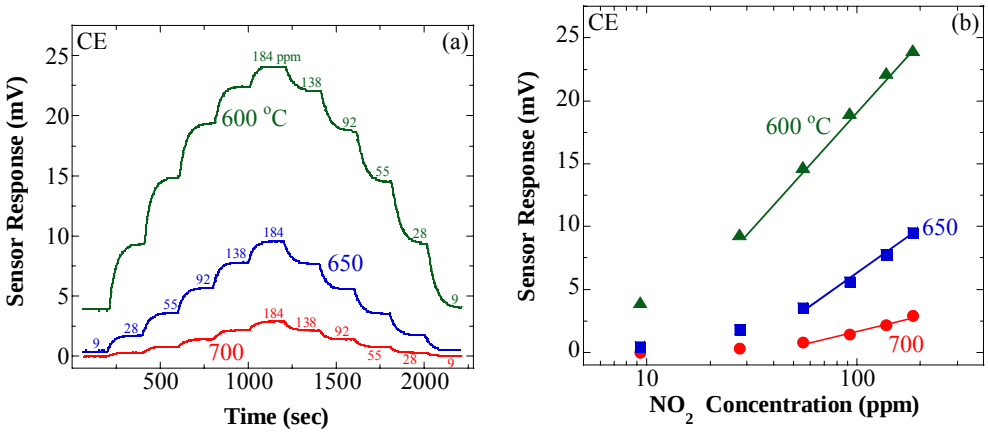

Fig. 41. NO_2 sensitivity of CeO_2-based sensor (CE) in 21 % O_2 and balance N_2 at 600 to 700 ºC. (a) Plots of sensor emf vs. time. NO_2 concentrations are shown for each step in ppm and (b) Plots of sensor emf vs. NO_2 concentration. The lines drawn in (b) are logarithmic fits.

4-3.3 Selectivity

NO_2 Selectivity against CO and CO_2

The effect of 0 to 400 ppm CO on the NO_2 sensitivity of the sensors was investigated in 21 % O_2 at 600 ºC (Fig. 42). All of the sensors were able to detect 10 to 200 ppm NO_2 selectively in the presence of 200 ppm CO. The sensor EMF values, with and without CO, were similar to each other at a given concentration step (maximum difference less than 1.0 mV).

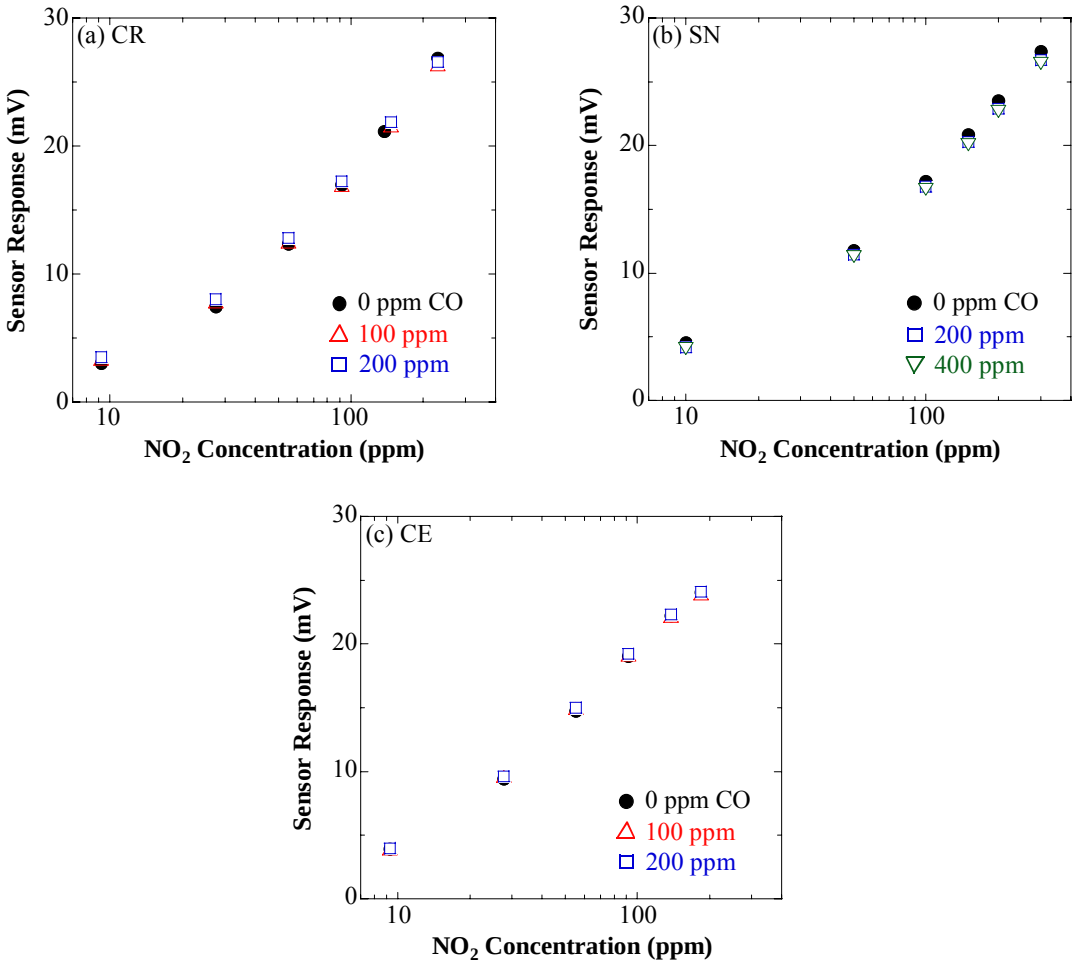

Fig. 42. Effect of CO on NO_2 sensitivity in 21 % O_2 with N_2 balance at 600 ºC. (a) Cr_2O_3-based sensor (CR), (b) SnO_2-based sensor (SN), and (c) CeO_2-based sensor (CE).

The effect of 10 to 20 % CO_2 was also negligible (Fig. 43). The sensors were all selective to NO_2 without a significant interference from CO_2. Upon the addition of CO_2 in 21 % O_2 at 600 ºC, a small decrease in the EMF values occurred but without a change in the slopes of the responses. The decrease was less than 1.5 mV for the Cr_2O_3 and CeO_2 sensor, and less than 2.5 mV for the SnO_2 sensor. These results are still within the general range of reproducibility.

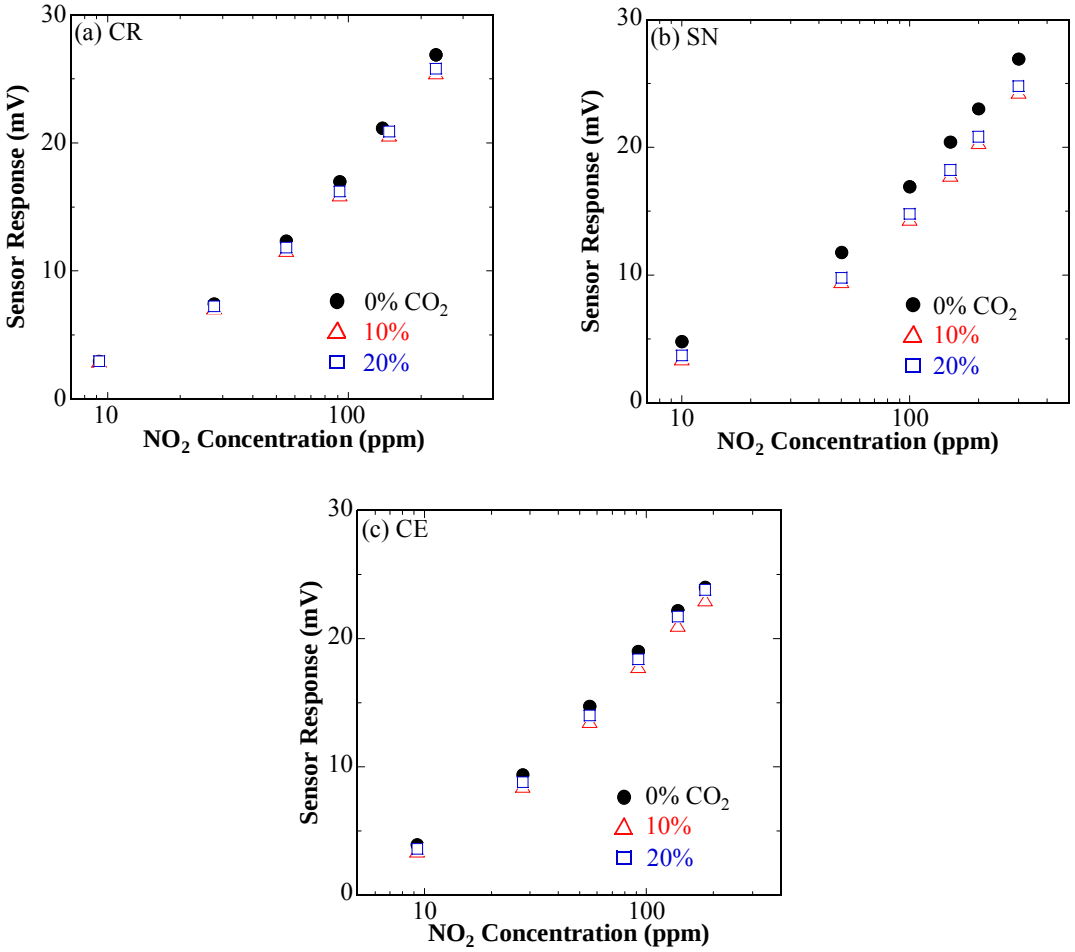

Fig. 43. Effect of CO_2 on NO_2 sensitivity in 21 % O_2 with N_2 balance at 600 ºC. (a) Cr_2O_3-based sensor (CR), (b) SnO_2-based sensor (SN), and (c) CeO_2-based sensor (CE).

NO_2 Selectivity against O_2, NO, and H_2O

The influence of O_2 on NO_2 sensitivity at 600 ºC is shown in Fig. 44. When O_2 concentration increased from 1 (or 3 %) to 21 %, both the EMF values and the response slopes decreased for all of the sensors. The slopes in 1 or 3 % O_2 were considerably higher than those in concentrations larger than 10 % O_2. However, the sign of the slopes remained the same over the entire range of O_2. The Cr_2O_3-, SnO_2-, and CeO_2-based sensors showed similar trends as the WO_3 sensor for the O_2 effect on NO_2 sensitivity. None of the sensors showed a response to a change in O_2 concentration in the absence of NO_2 (not shown). This implies that catalytic and/or adsorptive behavior associated with an O_2 response is symmetrical between the metal

oxide and Platinum electrodes. Higher O_2 concentrations might increase the O_2 contribution to the overall electrode reactions. This, in turn, may decrease the relative contribution of NO_2 to the electrode reactions and reduce the overall sensor response that is solely associated with NO_2.

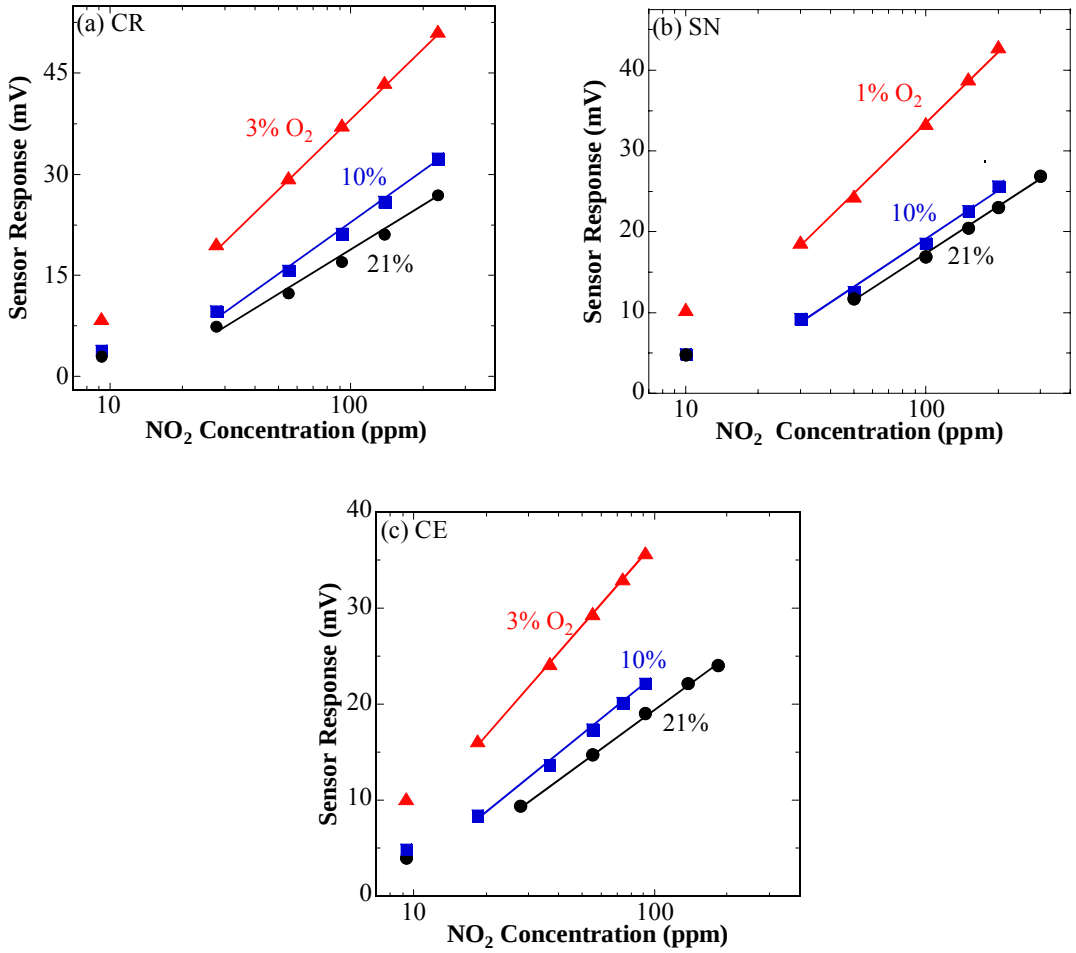

Fig. 44. Effect of O_2 on NO_2 sensitivity in N_2 balance at 600 ºC. (a) Cr_2O_3-based sensor (CR), (b) SnO_2-based sensor (SN), and (c) CeO_2-based sensor (CE). The lines are logarithmic fits.

The influence of NO on the NO_2 sensitivity was also significant. As seen in Fig. 45, the EMF values generally decreased with increasing NO concentration (0 – 300 ppm), resulting in a downward shift of the plots. This was likely due to the opposite response direction of the sensors to NO. For all of the sensors a small increase of the slope was seen upon the addition of 100 ppm NO. Furthermore, the sensors all had similar selectivity behavior as the WO_3

sensor. This NO effect implies that a thermodynamic equilibrium for NO_2 decomposition (8) was not established over the MO_x electrodes at 600 ºC [24].

$$NO_2 \leftrightarrow NO + \tfrac{1}{2}O_2 \tag{8}$$

If thermodynamic equilibrium were attained during NO_2 sensing, more than 80 % NO_2 would have been converted to NO at this temperature. As a result, there would have been a negative EMF due to non-electrochemically formed NO. However, a positive response is observed, indicating that this was not the case.

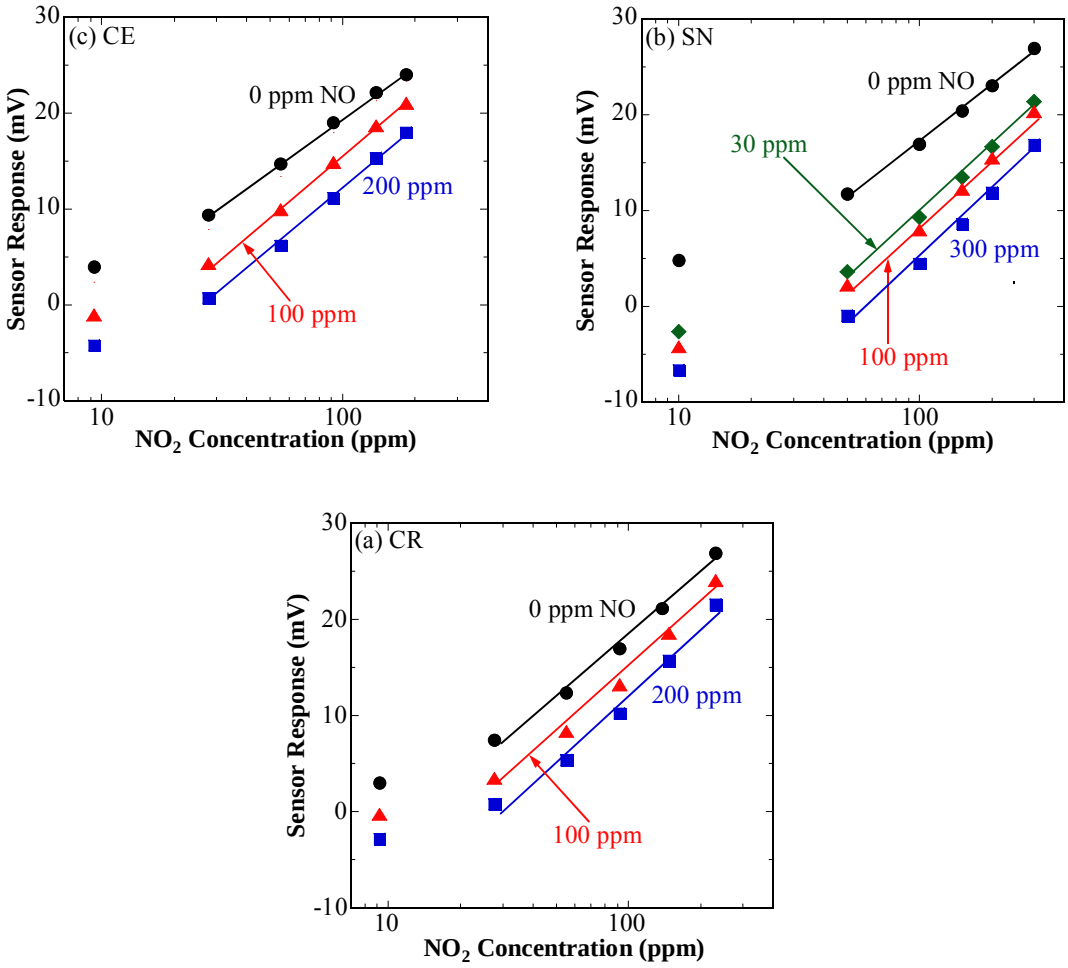

Fig. 45. Effect of NO on NO_2 sensitivity in 21 % O_2 with N_2 balance at 600 ºC. (a) Cr_2O_3-based sensor (CR), (b) SnO_2-based sensor (SN), and (c) CeO_2-based sensor (CE). The lines are logarithmic fits.

The effect of 3 % H_2O to NO_2 sensor response was also investigated (Fig. 46). An addition of 3 % H_2O significantly decreased both the slopes of the sensor response and the EMF values. The Cr_2O_3, SnO_2, and CeO_2 sensors all showed similar NO_2 selectivity over H_2O as the WO_3 sensor. A linear relationship was still seen between 50 and 200 ppm NO_2 in the presence of 3 % H_2O. This NO_2 selectivity is likely due to a similarity in the relative catalytic activity between the electrodes, with the Platinum being catalytically more active than the metal oxides [24].

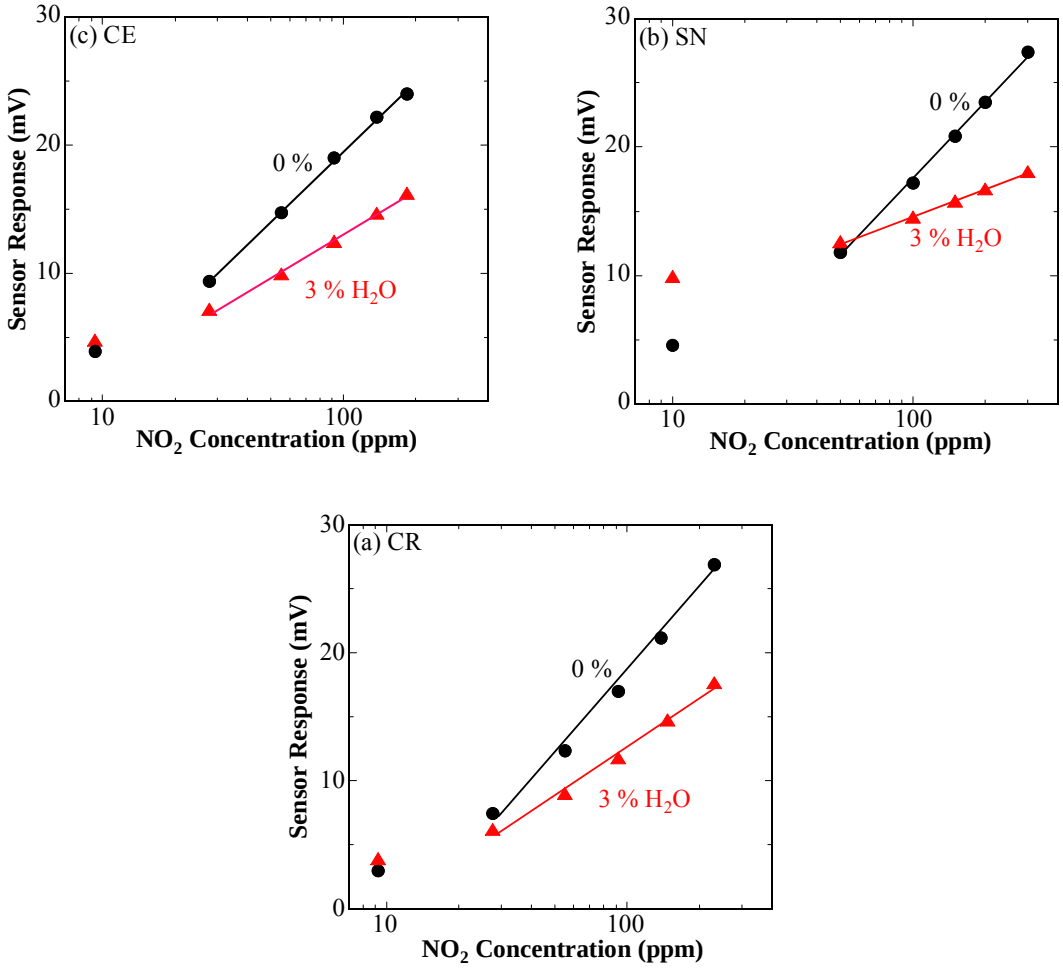

Fig. 46. Effect of H_2O on NO_2 sensitivity in 21 % O_2 with N_2 balance at 600 ºC. (a) Cr_2O_3-based sensor (CR), (b) SnO_2-based sensor (SN), and (c) CeO_2-based sensor (CE). The lines are logarithmic fits.

4-3.4 Sensing Properties in Simulated Exhaust

The NO_2 response in 3 % O_2 (N_2 balance) and in the same simulated exhaust conditions as described in previous sections were compared for the Cr_2O_3- and CeO_2-based sensor at 600 ºC (Fig. 47). The sensor EMF values and slopes of the responses measured in the simulated exhaust were generally lower than in 3 % O_2 for both sensors. The behavior of the sensors in the simulated exhaust gas resembles that of the addition of 3 % H_2O in 21 % O_2 (Fig. 46). This indicates that having water in the gas stream has a major effect on the NO_2 sensing behavior over CO_2 and CO.

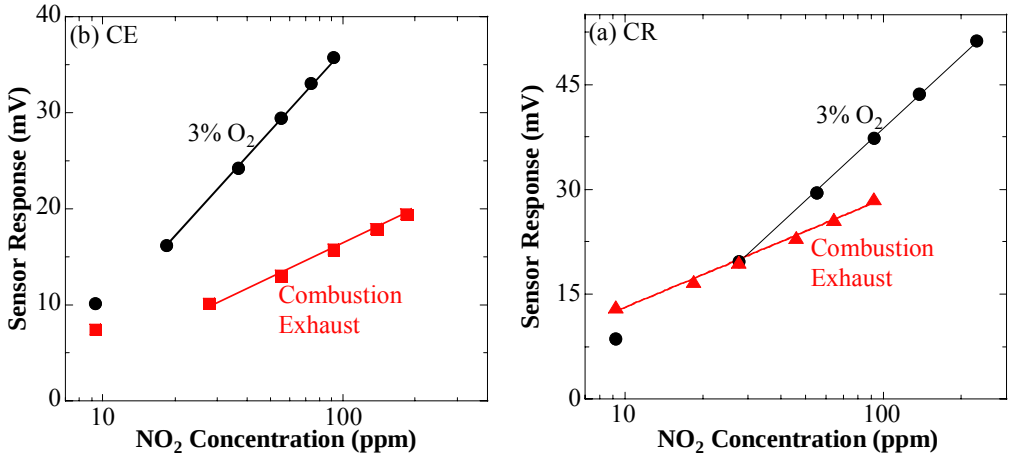

Fig. 47. Comparison of NO_2 sensitivity between in 3 % O_2 and in simulated exhaust (3 % O_2, 3 % H_2O, 16 % CO_2, and 100 ppm CO) at 600 ºC. (a) Cr_2O_3-based sensor (CR) and (b) CeO_2-based sensor (CE). The lines are logarithmic fits.

4-4. Multifunctional Sensor

4-4-1. Fabrication of Tape-Cast YSZ Substrates

8 mol % YSZ substrates were fabricated for use in the multifunctional gas sensor. The substrates were tape-cast using a lab-scale table top continuous tape caster (Fig. 4). Fig. 48(a) shows the resulting YSZ green tapes on the carrier films used during the tape-casting technique. The YSZ green tape was cut to the desired size for the sensor substrates and sintered at 1450°C for 4 hours. The sintered YSZ substrates are shown in Fig. 48(b).

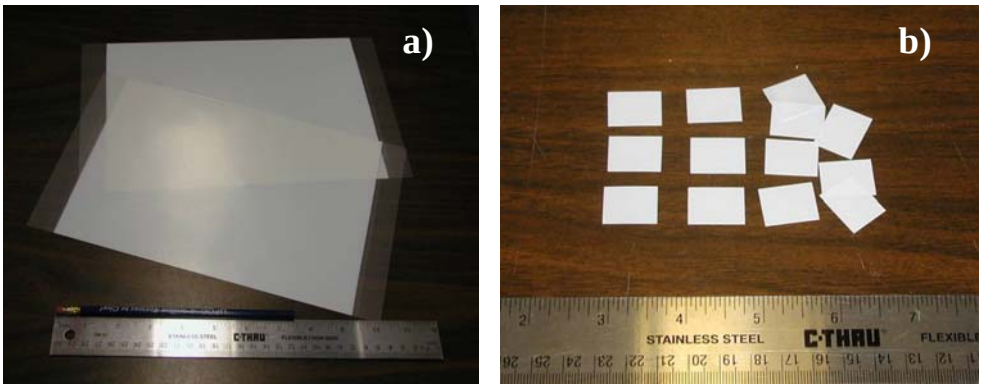

Fig. 48. Results of tape casting for multifunctional gas sensor. (a) YSZ green tapes and (b) sintered YSZ substrates using the tape.

4-4-2. Multifunctional Gas Sensor Array Results

Multifunctional sensors with integrated heating elements were fabricated and tested. The sensors consisted of an array of three sensing electrodes (two La_2CuO_4 electrodes and one Platinum electrode) deposited on thin YSZ substrates with C-shaped Pt heating elements directly opposite the sensing electrodes (Fig. 5). Platinum elements acted as both a local heater for one sensing electrode (LCO1) and also as temperature sensors for the three sensing electrodes. The temperature distribution within the sensor was modeled using Finite Element Modeling (FEM). Good selectivity for NO_2 vs. NO was achieved by adjusting the temperature of one of the sensing electrodes. The small prototype device with lead wires attached can be seen in Fig. 49.

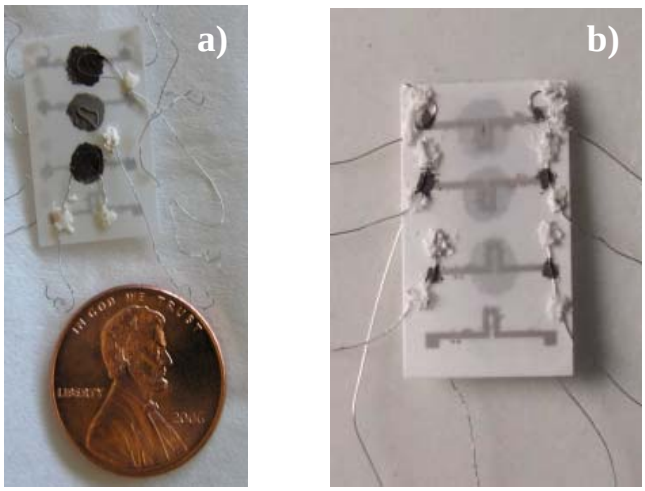

Fig. 49. Small prototype multifunctional gas sensor array with lead wires attached. (a) Top of sensor array with two La_2CuO_4 sensing electrodes and single Pt reference electrode. (b) Bottom of device showing the attachment of lead wires to 3 out 4 Pt elements. Refer to Fig. 5 for additional information.

The temperature distribution in the sensor was calculated with FEM (MatLab 7.0). Average values for material parameters, such as the thermal conductivity of YSZ, were taken from literature. Heat transfer coefficients for the system were calculated from experimental data and agreed well with typical values from literature. These parameters were used in the model to determine the temperature distribution under actual operating conditions with voltage applied to the heating element. The model predictions were checked with external thermocouples and compared to calculated temperatures using custom software (Labview 7.1) and resistance measurements of the Platinum elements. These calculations were based on previously measured Platinum resistance vs. temperature data, which were fit to a mathematical model.

The curve fits (not shown) for the Platinum elements were very good (R^2=1) and allowed accurate determination of the surface temperatures. An initial experiment was used to verify that the Platinum heating elements were calibrated successful. The furnace was ramped to several different temperature setpoints with no voltage being applied to the Platinum heating element aligned with LCO1. An example of the results from these verification trials is shown in Fig. 50. In this plot LCO1, LCO2, and Pt represent the temperature under each of the three sensing electrodes (see Fig. 5). These temperatures were calculated with custom software using algorithms from the calibration and the measured resistance values of the Platinum elements as

the furnace ramped. As evident in the plot, the calculated temperature of the Platinum elements was very accurate. Deviation from the actual furnace temperature was greatest during furnace ramps but never exceeded ± 3 °C. This deviation was most likely a result of the finite time required for the Platinum to absorb heat. Temperatures remained constant during all tests for a given furnace setpoint.

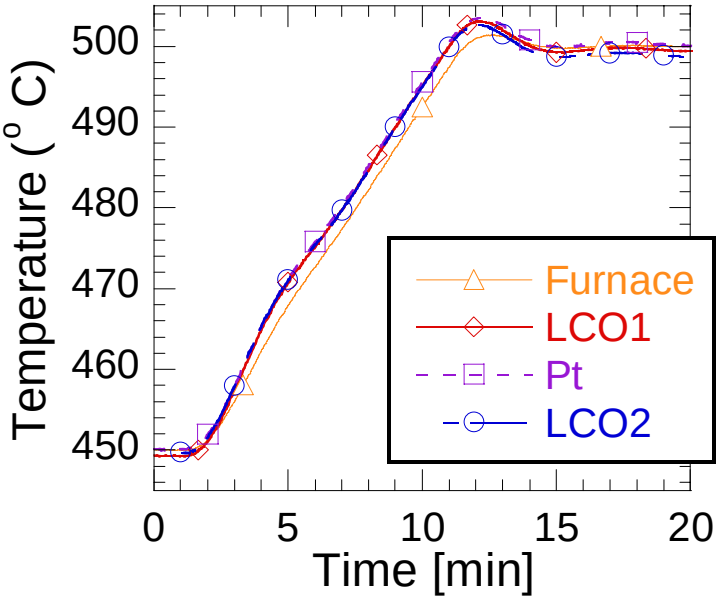

Fig. 50. Verification of Platinum element calibration and quality of curve fits.

An initial analysis indicated that a 2-D thermal analysis was sufficient in this case because the sensor array was very thin (0.1 mm). In other words, the temperature on the top and bottom of the array was almost identical. The surface temperature distribution was estimated at a heater voltage of 3.5 V (~515 °C) with a background furnace temperature of 450 °C and is shown in Fig. 51. The results give a 2-D representation of the heat dissipating through the sensor and to the gas environment away from an active heating element. Thermal modeling was helpful in determining where stress concentrations are located. The FEM was also useful for considering how close to place each of the sensing elements and heating elements so that each was placed at an optimum temperature [27].

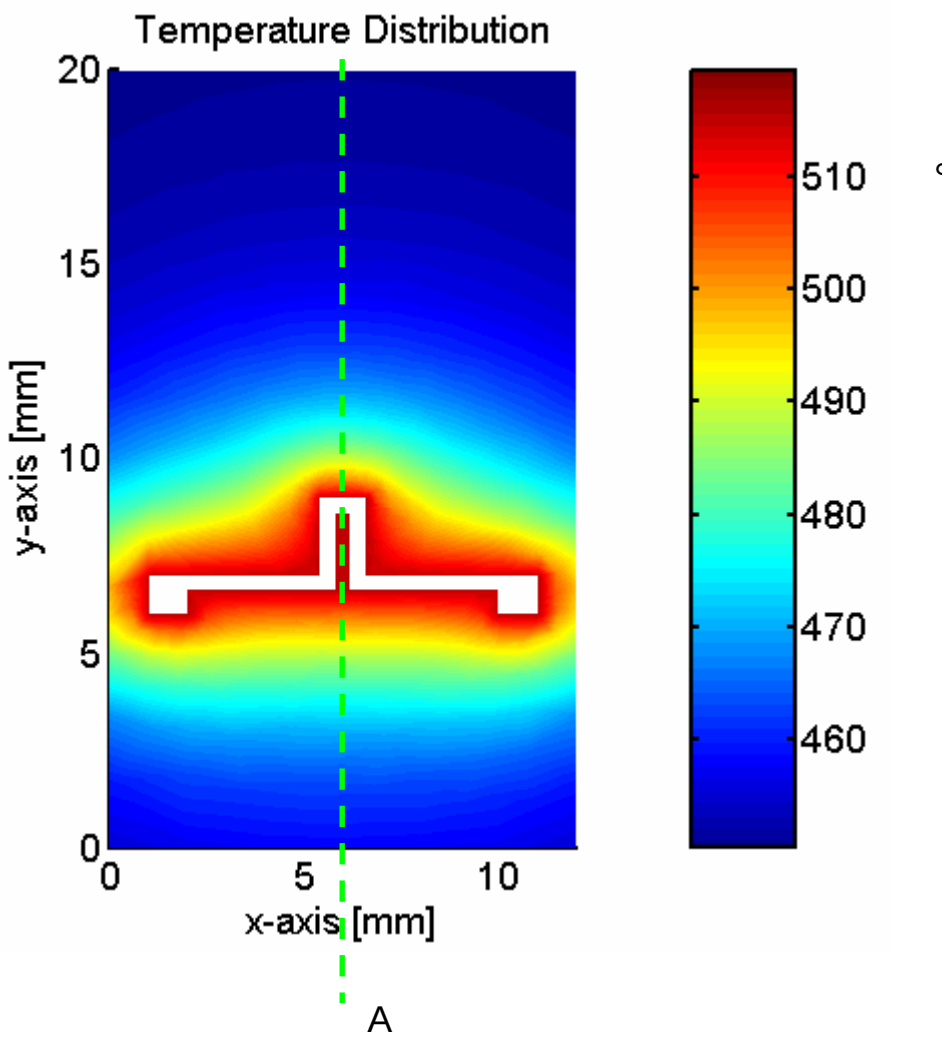

Fig. 51. Surface temperature profile for a C-shaped Pt heating element deposited on a thin YSZ substrate as calculated with Finite Element Modeling. Background furnace temperature = 450 °C, 3.5 V applied to heating element for Joule heating of NO_x sensing element.

The temperatures of the sensing electrodes and the power delivered to the heating element (under LCO1) at three voltage setpoints were estimated from experimental data and are given in Table 3. The temperatures came from the calculations based on resistance measurements of the Platinum elements.

Setpoint	Applied Voltage	Heater Power	T_{LCO1}	T_{Pt}	T_{LCO2}
1	1.5 V	70 mW	460°C	452°C	450°C
2	2.5 V	185 mW	484°C	454°C	451°C
3	3.5 V	360 mW	515°C	457°C	452°C

Table 3. Surface temperatures and heater power for the application of three different voltages to the Pt heating element.

The FEM results agreed closely with the measured values (T_{LCO1}, T_{Pt}, and T_{LCO2}) in Table 3, which represent average temperatures for the C-shaped Platinum elements. The temperature profile along the A-A' axis (Fig. 5) is shown in Fig. 52. This plot is taken from the FEM with the heater temperature at a uniform 515 °C. The temperature was highest for sensing electrode LCO1 which was aligned with the heater. The temperature remains fairly constant at the heater and LCO1 electrode, and drops off rapidly as distance from the heater increases as was shown in Fig. 51.

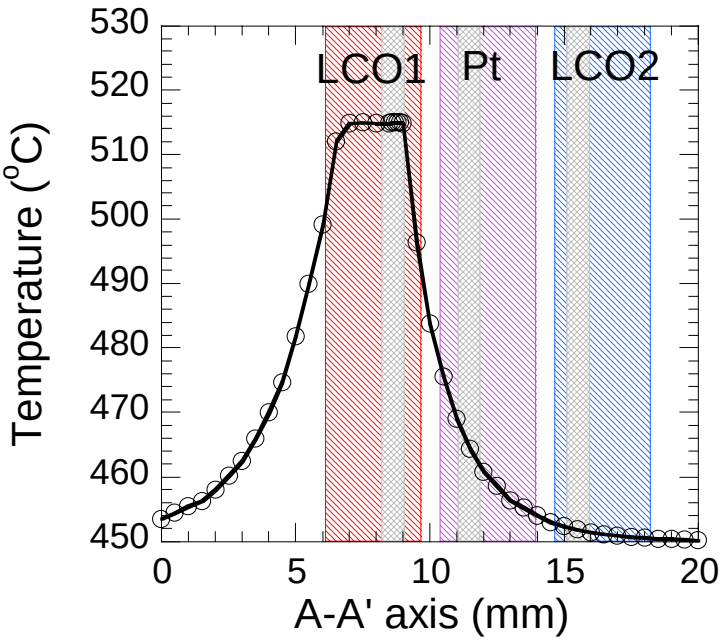

Fig. 52. Temperature profile along the A-A' axis from FEM. Also shown are the locations of the sensing electrodes (diagonal, down to right) and Platinum elements (cross-hatch).

Fig. 53 shows the steady-state sensitivity plots for LCO1 (actively heated) and LCO2 (at furnace temp) versus the Platinum reference electrode (also at furnace temp) for NO and NO_2 concentration (0, 50, 100, 200, 400, and 650 ppm) steps. The voltage baseline for the heated La_2CuO_4 electrode vs. Pt response (LCO1 in Fig. 53(a) and (b)) shifted up as the temperature was increased locally with the heating element. Conversely, the voltage baseline for the unheated La_2CuO_4 electrode vs. Pt response (LCO2 in Fig. 53(c) and (d)) remained around 0 mV regardless of the heating occurring at the LCO1 electrode. The baseline voltage shifted from approximately 15 mV to 50 mV as the temperature difference between the LCO1 and Platinum electrodes increased from 8 to 30 °C. There was also a change from 50 mV to 90 mV as the temperature difference between the electrodes increased to 65 °C. This offset from the expected value of zero was most likely a result of the difference in electrode temperatures. This can be explained with the Nernst equation

$$E = \frac{RT}{4F}\ln\left(\frac{p_{O_2}^{LCO}}{p_{O_2}^{Pt}}\right) = \frac{RT}{4F}\ln\left(p_{O_2}^{LCO}\right) - \frac{RT}{4F}\ln\left(p_{O_2}^{Pt}\right) \quad (9)$$

where, for an unheated sensor, the oxygen concentrations and the temperatures for the LCO and Platinum electrodes are equal and therefore the potential (E) is zero [27].

The responses were positive for NO at all concentrations but saturated at higher values. This occurred even when all electrodes were at the same temperature (not shown) and was possibly a result of electrode preparation. For NO_2 the responses were negative at low concentrations and became positive at higher concentrations. As the heater temperature increased, the NO sensitivity for the LCO1-Pt signal decreased to zero. However, the signal still remained sensitive to NO_2. The LCO2-Pt signal had a similar sensitivity to NO_2 as LCO1-Pt, although interestingly showed an improved sensitivity to NO as the heater temperature increased. These prototype experiments demonstrated that the manipulation of NO_x sensitivities and selectivities with integrated heating elements is a practical method for operating effective NO_x sensing arrays.

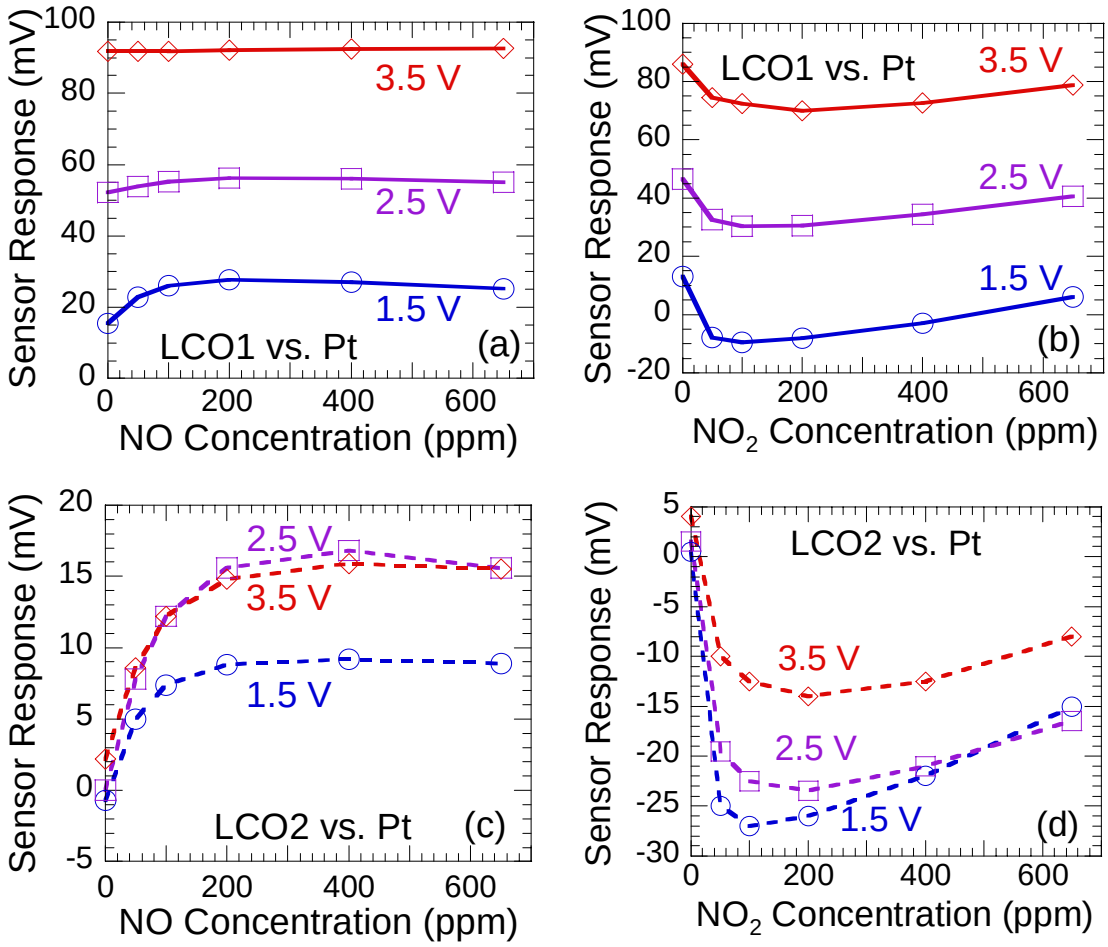

Fig. 53. La_2CuO_4 electrode potential as a function of heater voltage setpoint. LCO1(Hot) vs. Pt(at furnace temp) is shown in (a) and (b) for NO and NO_2, respectively. The response of LCO2(at furnace temp) vs. Pt(at furnace temp) is shown in (c) for NO and (d) for NO_2. See Table 3 for the corresponding electrode temperatures for each setpoint.

The decreasing sensitivity of LCO1-Pt to NO as the heater temperature increased is an improvement over an unheated sensor. As shown in this report, sensors with unheated La_2CuO_4 and Pt electrodes typically respond to both NO and NO_2 in nearly the same temperature range. This creates a problem for selectively identifying and independently measuring the concentration of either NO or NO_2 in a mixture of NO_x. However, this sensor array did not have this problem because the LCO1 vs. Pt and the LCO2 vs. Pt signals were separated enough from one another to allow the unambiguous determination of NO and NO_2 concentrations with linear algorithms.

In summary, a multifunctional gas sensor array with an integrated Platinum heater and temperature sensors was fabricated, resulting in a device that is small in size and power-consumption. As an initial trial, two La_2CuO_4 electrodes were used as NO_x sensing elements. The heater and temperature sensor performance were verified with Finite Element Modeling and experimental data obtained with custom software. The selectivity of an individual sensing electrode was improved with local heating. When coupled with other sensing electrodes at different temperatures, a gas sensor array enables the unambiguous detection of NO and NO_2. In fact, additional sensing electrodes can be added to the array to detect additional species (e.g., CO). The multifunctional gas sensor array has reference and sensing electrodes in the same environment, allowing coplanar electrodes and, thus, avoiding complex designs which increase manufacturing costs.

4.5 Commercialization

Emissions Detection Technologies, Inc. (a subsidiary of Fuel FX International, Inc.) licensed the sensor technology from the University of Florida. They are committed to commercializing this technology and have raised venture capital resources to develop sensor prototypes. These prototypes are being fabricated and tested. Once complete, Fuel FX will pursue existing relationships with Original Equipment Manufacturer (OEM) suppliers and negotiate license agreements for mass-scale manufacturing of the sensor.

5. CONCLUSION

Solid state sensors were developed for coal combustion control and the understanding of their sensing mechanisms was advanced. Several metals and semiconducting metal-oxides (both p-type and n-type) were used to fabricate sensor electrodes. The adsorption/desorption characteristics and catalytic activities of these materials were measured with Temperature-Programmed-Desorption (TPD) and Temperature-Programmed-Reaction (TPR). The proposed sensing mechanism Differential Electrode Equilibria was verified and demonstrated by relating the sensing behavior (sensitivities and cross-sensitivities) of the various electrode materials to their gas adsorption/desorption behaviors and catalytic activities. This aspect of the work resulted in 12 scientific publications (Table 4).

The NO_x sensors based on La_2CuO_4 were tested in simulated exhaust gas environment containing N_2, CO_2, H_2O, O_2, CO, and NO_x. These sensors showed high selectivity toward NO_x, and NO sensitivity (voltage response) increased with decreasing temperature from 600 to 400 ºC. At lower temperatures the sensor response was limited by slow, unstable heterogeneous kinetics. This limits the sensor operation to temperatures above 400 °C. The TPD results showed that NO does not fully desorb from the surface of metal oxide until this temperature. Therefore, the instability of sensor response at low temperature might be explained as the saturation of the metal oxide surface with NO. That is, below 400 °C the rate of NO adsorption is greater than the rate of NO desorption. Above 400 °C, the rate of NO desorption is greater than the rate of NO adsorption. Any surface NO species are now directly proportional to the gas-phase composition. Between 400 and 600 °C the sensing mechanism is dominated by adsorbed NO species that are not in full equilibrium with the gas phase composition. The lack of any NO_2 from co-adsorbed NO and O_2 means that there were no electrochemical reactions. This would tend to indicate that the sensor response was not due to the conventional Mixed Potential theory. Therefore, the sensor response is most likely a result of changes in the semiconducting properties (i.e., Fermi level) rather than heterogeneous kinetics (i.e., Mixed Potential).

In contrast to the p-type La_2CuO_4-based sensors, positive voltage responses were seen for NO_2 and negative ones for NO at 650 ºC when using n-type semiconducting WO_3-based

sensors. A linear relationship was obtained in the plot of the sensor voltage vs. the logarithm of NO_x concentration for both NO and NO_2. The WO_3-based sensor responded highly to about 10 ppm NO_2 and selectively in the existence of CO, CO_2, and H_2O, showing it to be applicable to the monitoring of NO_2. H_2O and CO both had an effect on the NO sensitivity but not on NO_2 sensitivity in a 3 % O_2 environment. This shows that the WO_3-based sensor can be used to detect about 10 ppm NO_2 selectively. The sensor response to NO in simulated exhaust gas was considerably different from that in 3 % O_2. This difference indicated a possible gas composition change at 650 ºC and possibly the formation of a hydroxylated surface by water vapor in combustion exhaust streams. The NO_2 sensitivity also changed in simulated exhaust gas but not as significantly.

The NO_x selectivity of Cr_2O_3, SnO_2, and CeO_2 electrodes were also measured. The NO_2 sensitivities of all three of the electrode materials were unaffected by CO or CO_2. However, the NO_2 sensitivity of the electrodes changed significantly when the concentrations of either O_2 or moisture were changed.

The effect of electrode grain size on NO_x sensitivity and response time was investigated using a La_2CuO_4-based potentiometric sensor. La_2CuO_4 powders, synthesized with four different routes, had different specific surface areas which lead to different morphologies of the sintered sensing electrodes. Large surface area powders generated porous electrode morphologies with small grain sizes. Furthermore, fine-grained electrodes exhibited sharper, faster responses when compared to coarse-grained electrodes.

A multifunctional sensor was fabricated and demonstrated in NO_x containing atmospheres. The sensor was fabricated via tape-casting, screen-printing, and sintering in air. A local heating structure and temperature sensors were incorporated into the sensor design using additional screen-printing and sintering steps. The prototype sensor array contained two sensing electrodes, the voltages of which were both referenced to a porous Pt electrode. NO sensitivity was reduced to zero while retaining normal NO_2 sensitivity via local heating of one of the La_2CuO_4 electrodes. The other La_2CuO_4 electrode remained sensitive to both NO and NO_2. With the use of simple algorithms, a low power gas sensor array enables the unambiguous

detection of individual gas constituents when using multiple sensing electrodes at different temperatures.

The sensor technology was licensed to Fuel FX International, Inc. Fuel FX has obtained investor funding and is developing prototype sensors as a first step in their commercialization strategy for this technology.

Table 4. Scientific Publications Resulting From This Contract

1. "Influence of Adsorption and Catalytic Reaction on Sensing Properties of a Potentiometric La_2CuO_4/YSZ/Pt Sensor," J. Yoo, S. Chatterjee, F. M. Van Assche, and E. D. Wachsman, *Journal of the Electrochemical Society*, **154**, J190 (2007).

2. "NO_2/NO Response of Cr_2O_3- and SnO_2-Based Potentiometric Sensors and Temperature-Programmed Reaction Evaluation of the Sensor Elements," J. Yoo and E. D. Wachsman, *Sensors & Actuators: B. Chemical*, **123**, 915-921 (2007).

3. "Sensing Properties and Selectivities of a WO_3/YSZ/Pt Potentiometric NO_x Sensor," J. Yoo, S. Chatterjee, and E. D. Wachsman, *Sensors & Actuators: B. Chemical*, **122**, 644-652 (2007).

4. "A Theoretical Framework for Prediction of Solid State Potentiometric Gas Sensor Behavior," B. M. White, E. Macam, F. M. Van Assche, E. Traversa and E. D. Wachsman, *Chemical Sensors 7 and MEMS/NEMS 7, ECS Transactions*, G. Hunter, S. Akbar, S. Bhansall, O. Brand, C. Bruckner-Lea, M. Carter, J. Davidson, E. Enlkov, P. Hesketh, R. Hillman, C. Kranz, J. Li, R. Maboudian, R. Mukundan, C. Roper, S. Shoji, A. Simonian, and M. Tabib-Azar, Ed., **3-10**, 179-194 (2006).

5. "Sensing Properties of MO_x/YSZ/Pt (MO_x = Cr_2O_3, SnO_2, CeO_2) Potentiometric Sensor for NO_2 Detection," J. Yoo, H. Yoon and E. D. Wachsman, *Journal of the Electrochemical Society*, **153**, H217-H221 (2006).

6. "Temperature-Programmed Reaction and Desorption of the Sensor Elements of a WO_3/YSZ/Pt Potentiometric Sensor," J. Yoo, F. M. Van Assche, and E. D. Wachsman, *Journal of the Electrochemical Society*, **153** (6), H115-121 (2006).

7. "Non-Nernstian Planar Sensors Based on YSZ with an Nb_2O_5 Electrode: Discussion on Sensing Mechanism," L. Chevallier, E. Di Bartolomeo, M. L. Grilli, M. Mainas, B. White, E. D. Wachsman, and E. Traversa, *Solid State Ionic Devices IV, ECS Transactions*, E.D. Wachsman, F.H. Garzon, E. Traversa, R. Mukundan, and V. Birss, Ed., **1-7**, 163-172 (2006).

8. "Electrical Characterization of Semiconducting La_2CuO_4 for Potentiometric Gas Sensor Applications," B. M. White, F.M. Van Assche, E. Traversa and E. D. Wachsman, *Solid State Ionic Devices IV, ECS Transactions*, E.D. Wachsman, F.H. Garzon, E. Traversa, R. Mukundan, and V. Birss, Ed., **1-7**, 109-120 (2006).

9. "Optimization of La_2CuO_4 Sensing Electrodes for a NO_x Potentiometric Sensor," E.R. Macam, F.M. Van Assche, J. Yoo and E. D. Wachsman, *Solid State Ionic Devices IV, ECS Transactions*, E.D. Wachsman, F.H. Garzon, E. Traversa, R. Mukundan, and V. Birss, Ed., **1-7**, 121-130 (2006).

10. "Heterogeneous Catalytic Evaluation of Potentiometric La_2CuO_4 Sensor Electrodes," F.M. Van Assche, J. Yoo, S. Chatterjee and E. D. Wachsman, *Solid State Ionic Devices IV, ECS Transactions*, E.D. Wachsman, F.H. Garzon, E. Traversa, R. Mukundan, and V. Birss, Ed., **1-7**, 185-200 (2006).

11. "Potentiometric NO_x Sensing Behavior, of Cr_2O_3-Based Sensor and TPR of the Sensor Element," J. Yoo and E. D. Wachsman, *Solid State Ionic Devices IV, ECS Transactions*, E.D. Wachsman, F.H. Garzon, E. Traversa, R. Mukundan, and V. Birss, Ed., **1-7**, 173-184 (2006).

12. "Multifunctional Potentiometric Gas Sensor Array With an Integrated Heater and Temperature Sensors," B. M. Blackburn, B. White, and E. D. Wachsman, 31st International Conference on Advanced Ceramics and Composites, (2007), accepted..

6. REFERENCES

1. T. Inoue, K. Ohtsuka, Y. Yoshida, Y. Matsuura, and Y. Kajiyama, Metal Oxide Semiconductor NO_2 Sensor, *Sensors and Actuators B*, **24-25**, (1995), 388-391.

2 Y. Wu, Z. Zhao, Y. Liu, and X. Yang, The Role of Redox Property of $La_{2-x}(Sr,Th)_xCuO_{4-\delta}$ Playing in the Reaction of NO Decomposition and NO Reduction by CO, *J. of Mol. Cat. A: Chemical*, **155**, (2000), 89-100.

3. H. Oshima, M. Tatemichi, and T. Sawa, Chemical Basis of Inflammation Induced Carcinogenesis, *Archives of Biochemistry and Biophysics*, **417**, (2003), 3-11.

4. F. Ménil, V. Coillard, and C. Lucat, Critical Review of Nitrogen Monoxide Sensors for Exhaust Gases of Lean Burn Engines, *Sensors and Actuators B*, **67**, (2000), 1-23.

5. M. J. Madou and S.R. Morrison, Chemical Sensing with Solid State Devices, Academic Press. (1989).

6. M. L. Grilli, E. Di Bartolomeo, A. Lunardi, L. Chevallier, S. Cordiner, and E. Traversa, Planar Non-Nernstian Electrochemical Sensors: Field Test in the Exhaust of a Spark Ignition Engine, *Sensors and Actuators B-Chemical,* **108** (2005) 319-325.

7. B. M. White, E. Macam, F. M. Van Assche, E. Traversa, and E. D. Wachsman, A Theoretical Framework for Predicting Solid-State Potentiometric Gas Sensor Behavior pp 179. in Proceedings of the 210th Meeting of The Electrochemical Society, Vol. 3, *Chemical Sensors 7 - and MEMS/NEMS 7, ECS Transactions.* Edited by G. Hunder, S. Akbar, S. Bhansali, O. Brand, C. Bruckner-Lea, M. Carter, J. Davidson, E. Enikov, P. Hesketh, R. Hillman, C. Kranz, J. Li, R. Maboudian, R. Mukundan, C. Roper, S. Shoji, A. Simonian, and M. Tabib-Azar. The Electrochemical Society, Pennington, NJ, 2006.

8. E. D. Wachsman and P. Jayaweera, *Solid State Ionic Devices II - Ceramic Sensors, The Electrochem. Soc. Proceedings* 2001, E.D. Wachsman, W. Weppner, E. Traversa, M. Liu, P. Vanysek, and N. Yamazoe, Ed., **2000-32**, 298-304.

9. E. Di Bartolomeo, M.L. Grilli, and E. Traversa, *Solid State Ionic Devices III, The Electrochem. Soc. Proceedings* 2003, E. D. Wachsman, K. Swider-Lyons, M. F. Carolan, F. H. Garzon, M. Liu, and J. R. Stetter, Ed. **2002-26**, 222-235.

10. E.D. Wachsman, *Solid-State Ionic Devices III, The Electrochem. Soc. Proceedings*, 2003, E. D. Wachsman, K. Swider-Lyons, M. F. Carolan, F. H. Garzon, M. Liu, and J. R. Stetter, Ed., **2002-26**, 215-221.

11. E. Di Bartolomeo, N. Kaabbuathong, M.L. Grilli, and E. Traversa, Planar Electrochemical Sensors Based on Tape-Cast YSZ Layers and Oxide Electrodes, *Solid State Ionics*, **171**,

(2004), 173-181.

12. E. Traversa, A. Bearzotti, M. Miyayama, and H. Yanagita, Influence of the Electrode Materials on the Electrical Response of ZnO-based Contact Sensors, *J. of the European Ceramic Society*, **18**, (1998), 621-631.

13. N. Miura, T. Raisen, G. Lu, and N. Yamazoe, Highly Selective CO Sensor Using Stabilized Zirconia and a Couple of Oxide Electrodes, *Sensors and Actuators B*, **47**, (1998), 84-91.

14. G. Lu, N. Miura, and N. Yamazoe, Stabilized Zirconia-Based Sensors Using WO_3 Electrode for Detection of NO or NO_2, *Sensors and Actuators B*, **65**, (2000), 125-127.

15. A. Dutta, N. Kaabbuathong, M. L. Grilli, E. Di Bartolomeo, and E. Traversa, Study of YSZ-Based Electrochemical Sensors with WO_3 Electrodes in NO_2 and CO Environments, *J. Electrochem. Soc.*, **150**, (2003), H33-H37.

16. J. Schafer, W. Sigmund, S. Roy, and F. Aldinger, Low Temperature Synthesis of Ultra fine P b(Zr,Ti)O_3 Powder by Sol-Gel Combustion, *Journal of Materials Research*, **12**(10) (1997), 2518-2521.

17. B.L. Kirkwood, T.S. Luhman, R.R. Stephenson, and M.M. Strasik, Method for Producing Superconducting Oxide Compounds, *United States Patent*, 6,559,103, May 6, 2003.

18. Y. Zhu, R. Tan, T. Yi S. Gao, C. Yan, and L. Cao, Preparation of Nanosized La_2CuO_4 Perovs kite Oxide Using an Amorphous Heteronuclear Complex as a Precursor at Low- Temperatur e, *Journal of Alloys and Compounds*, **311** (2000), 16-21.

19. D. Bhattacharya, L. C. Pathak, S. K. Mishra, D. Sen, and K. L. Chopra, Pyrophoric Synthesis Technique for Multicomponent High-Temperature Superconductors, *Appl. Phys. Lett.,* **57** (1990), 2145-2147.

20. K. D. Schierbaum, U. Weimar, W. Gopel, and R. Kowalkowski, Conductance, Work Function and Catalytic Activity of SnO_2-Based Gas Sensors, *Sens. Actuators B,* **3** (1991), 205-214.

21. S. Zhuiykov, M. Muta, T. Ono, M. Hasei, N. Yamazoe, and N. Miura, Stabilized Zirconia-Based NO_x Sensor Using $ZnFe_2O_4$ Sensing Electrode, *Electrochemical and solid-state letters*, **4**, (2001), H19-H21.

22. G. Lu, N. Miura, and N. Yamazoe, Mixed Potential Hydrogen Sensor Combining Oxide Ion Conductor with Oxide Electrode, *J. Electrochem. Soc.*, **143**, (1996), L154-L155.

23. N. Sakai, K. Yamaji, T. Horita, H. Kishmoto, Y. P. Xiong, and H. Yokokawa, Significant

Effect of Water on Surface Reaction and Related Electrochemical Properties of Mixed Conducting Oxides. *Solid State Ionics*, **175**, (2004), 387-391.

24. J. Yoo, F. M. Van Assche, and E. D. Wachsman, *J. Electrochem. Soc*., **153**(6) (2006) H115-H121.

25. I. Lundström, *Sensors and Actuators B*, **35-36** (1996) 11-19.

26. H. T. Sun, C. Cantalini, L. Lozzi, M. Passacantando, S. Santucci, and M. Pelino, *Thin Solid Films*, **287** (1996) 258-265.

27. B. M. Blackburn, B. White, and E. D. Wachsman, 31st International Conference on Advanced Ceramics and Composites, (2007), accepted.